Cell Reports

Article

Basal Suppression of the Sonic Hedgehog Pathway by the G-Protein-Coupled Receptor Gpr161 Restricts Medulloblastoma Pathogenesis

Graphical Abstract

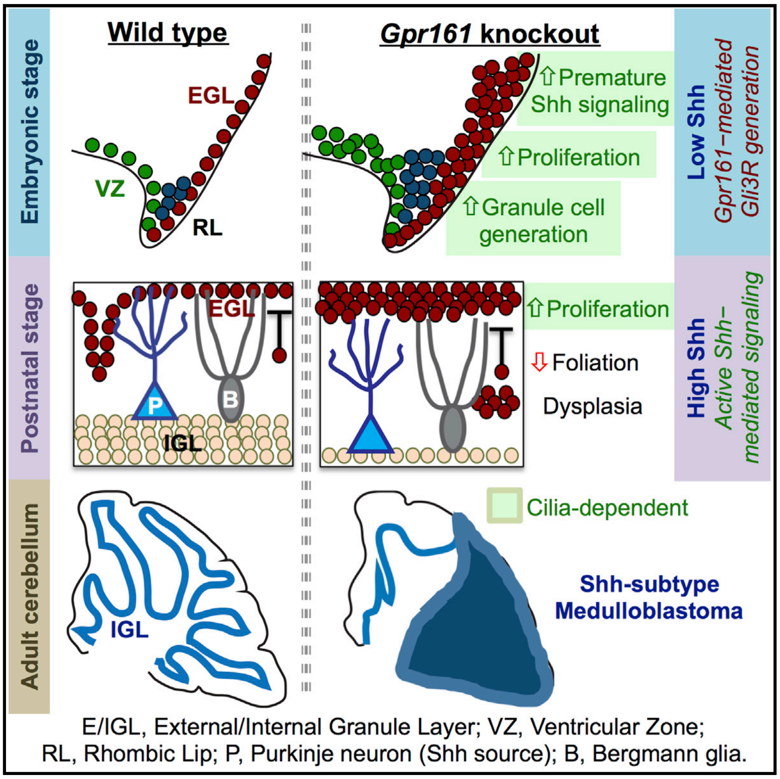

E/IGL, External/Internal Granule Layer; VZ, Ventricular Zone; RL, Rhombic Lip; P, Purkinje neuron (Shh source); B, Bergmann glia.

Authors

Issei S. Shimada, Sun-Hee Hwang, Bandarigoda N. Somatilaka, ..., Zhenyu Xuan, Michael D. Taylor, Saikat Mukhopadhyay

Correspondence

saikat.mukhopadhyay@utsouthwestern.edu

In Brief

Shimada et al. identify the ciliary G-protein-coupled receptor Gpr161 as a tumor suppressor in Shh subtype medulloblastoma. The authors suggest that Gpr161 restricts premature Shh pathway activity during granule cell progenitor development, implying that cilium-mediated pathway suppression preceding Shh signaling prevents tumorigenesis.

Highlights

- Gpr161 is a tumor suppressor in sonic hedgehog (Shh) subtype medulloblastoma (MB)
- Granule cell (GC) progenitor production increased upon *Gpr161* deletion and was cilium dependent
- Gpr161 restricted premature Shh pathway activity and GC progenitor overproduction in embryos
- Reduced *GPR161* expression correlated with poor survival of SHH-MB patients

Shimada et al., 2018, Cell Reports *22*, 1169–1184
January 30, 2018 © 2018 The Author(s).
https://doi.org/10.1016/j.celrep.2018.01.018

Cell Reports
Article

Basal Suppression of the Sonic Hedgehog Pathway by the G-Protein-Coupled Receptor Gpr161 Restricts Medulloblastoma Pathogenesis

Issei S. Shimada,[1] Sun-Hee Hwang,[1] Bandarigoda N. Somatilaka,[1] Xin Wang,[5] Patryk Skowron,[5] Jiwoong Kim,[2] Min Kim,[2] John M. Shelton,[3] Veena Rajaram,[4] Zhenyu Xuan,[6] Michael D. Taylor,[5] and Saikat Mukhopadhyay[1,7,*]
[1]Department of Cell Biology
[2]Department of Bioinformatics
[3]Department of Internal Medicine
[4]Department of Pathology and Laboratory Medicine, Children's Health
University of Texas Southwestern Medical Center, Dallas, TX 75390, USA
[5]Division of Neurosurgery, Hospital for Sick Children, Toronto, ON M5C 1X8, Canada
[6]Department of Biological Sciences, Center for Systems Biology, University of Texas at Dallas, Richardson, TX 75080, USA
[7]Lead Contact
*Correspondence: saikat.mukhopadhyay@utsouthwestern.edu
https://doi.org/10.1016/j.celrep.2018.01.018

SUMMARY

Sonic hedgehog (Shh) determines cerebellar granule cell (GC) progenitor proliferation and medulloblastoma pathogenesis. However, the pathways regulating GC progenitors during embryogenesis before Shh production by Purkinje neurons and their roles in tumorigenesis remain unclear. The cilium-localized G-protein-coupled receptor Gpr161 suppresses Shh-mediated signaling in the neural tube. Here, by deleting *Gpr161* in mouse neural stem cells or GC progenitors, we establish Gpr161 as a tumor suppressor in Shh subtype medulloblastoma. Irrespective of Shh production in the cerebellum, *Gpr161* deletion increased downstream activity of the Shh pathway by restricting Gli3-mediated repression, causing more extensive generation and proliferation of GC progenitors. Moreover, earlier deletion of *Gpr161* during embryogenesis increased tumor incidence and severity. GC progenitor overproduction during embryogenesis from *Gpr161* deletion was cilium dependent, unlike normal development. Low *GPR161* expression correlated with poor survival of SHH subtype medulloblastoma patients. Gpr161 restricts GC progenitor production by preventing premature and Shh-dependent pathway activity, highlighting the importance of basal pathway suppression in tumorigenesis.

INTRODUCTION

A fundamental question in biology is the mechanism by which morphogen signaling determines the development of neural stem cells (NSCs) and neuroprogenitors. A less appreciated aspect of this problem is the role cell-intrinsic factors play in basally suppressing morphogenetic pathways even before morphogen gradients are established. Granule cells (GCs) in the cerebellum are the most abundant neuronal type in the brain, constituting ~80% of human brain neurons (Herculano-Houzel, 2009). GC progenitors arise from atonal homolog 1 (*Atoh1*)-expressing cells in the upper rhombic lip (uRL) of the embryonic cerebellum (cerebellar anlage) starting from embryonic day 13 (E13) (Machold and Fishell, 2005; Wang et al., 2005). Sonic hedgehog (Shh) is a critical mitogen regulating GC progenitor proliferation (Dahmane and Ruiz i Altaba, 1999; Wallace, 1999; Wechsler-Reya and Scott, 1999). However, Shh is secreted by Purkinje neurons, starting only from E18.5, resulting in a postnatal growth spurt of GC progenitors (Corrales et al., 2004; Fuccillo et al., 2006; Huang et al., 2010; Kim et al., 2011; Lewis et al., 2004). The factors that regulate the generation and maintenance of GC progenitor pools during embryogenesis in the low Shh environment, and whether basal suppression of Shh signaling plays any role during these critical developmental stages, are not known.

Medulloblastoma is the most common malignant pediatric brain tumor that originates in the cerebellum. Recent molecular profiling of these tumors has resulted in its classification into four subgroups: Wnt, SHH, group 3, and group 4 (Northcott et al., 2011). Shh subtype medulloblastoma (SHH-MB) represents about 30% of the total number of medulloblastomas. It also constitutes the most common subgroup of medulloblastomas affecting infants (< 3 years) and adults (> 16 years) alike. Shh-MBs result from abnormal expansion of GC progenitors (Schüller et al., 2008; Yang et al., 2008). Following generation in the uRL, the GC progenitors migrate tangentially into the formative external granule layer (EGL), where they initiate proliferation in the outer EGL. Around E17, and before the spurt in postnatal proliferation, cerebellar folia start appearing. The GC progenitors proliferate multiple times postnatally in a Shh-dependent manner before exiting the cell cycle. The post-mitotic GCs extend axons chronologically forming the molecular layer (ML) and migrate radially along the Bergmann glia into their final location for maturation in the inner granule layer (IGL). Thus, the

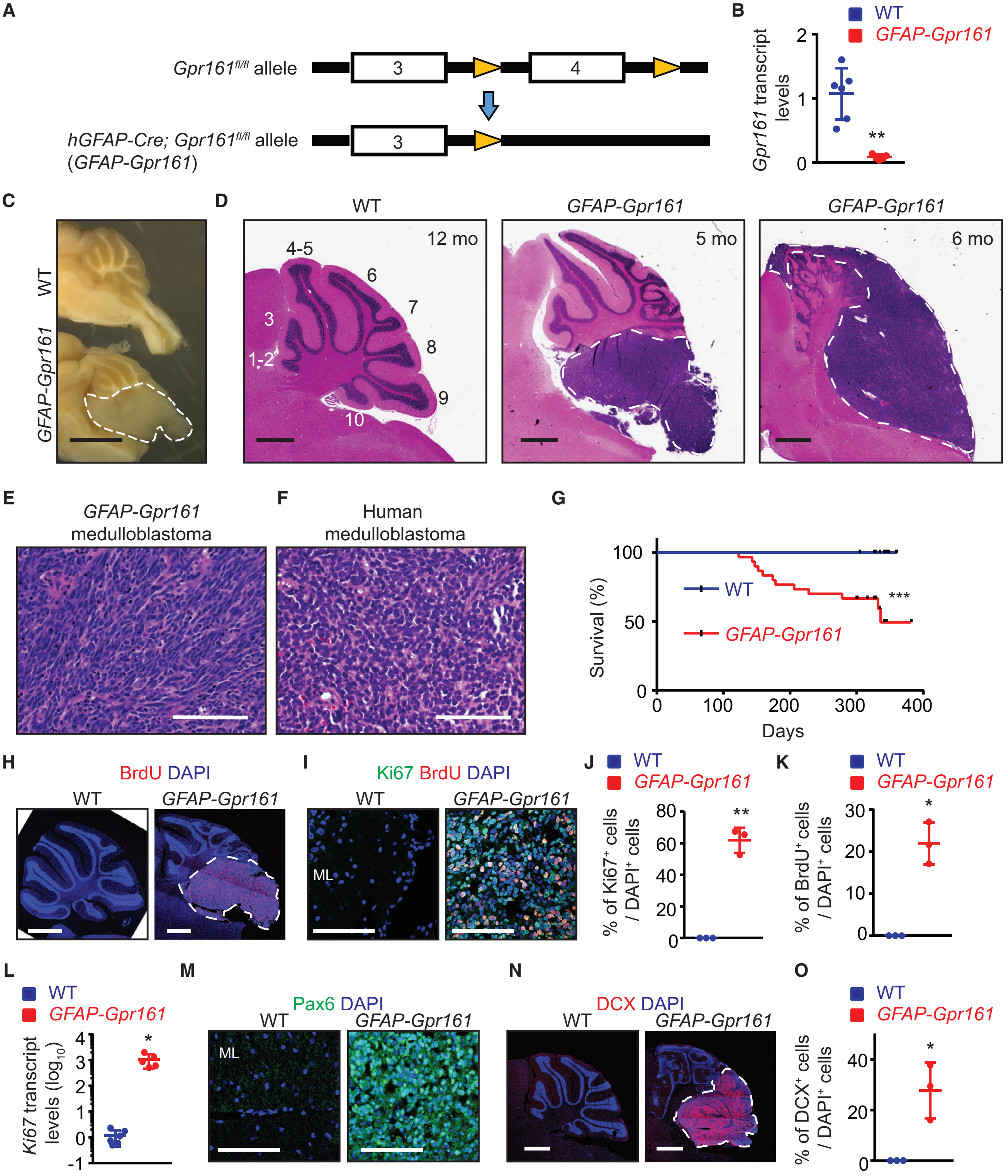

Figure 1. *Gpr161* Deletion in Neural Stem Cells Induces Cerebellar Tumorigenesis

(A) Schematic showing *Gpr161* exon 4 deletion with the *hGFAP-Cre* allele.

(B) *Gpr161* transcript levels in tumors of *GFAP-Gpr161* cko (*hGFAP-Cre; Gpr161*$^{fl/fl}$) mice (n = 5) are significantly decreased compared with the cerebellums of littermate controls designated as wild-type (WT) (*Gpr161*$^{fl/fl}$ or *Gpr161*$^{fl/+}$; n = 6) collected from 3- to 5-month-old mice.

(legend continued on next page)

pathogenesis of Shh-MB can be best understood in the context of normal development of GCs (Leto et al., 2016).

GC progenitors in the postnatal EGL are known to be ciliated (Spassky et al., 2008), and Shh-mediated proliferation at this stage is cilium dependent (Chizhikov et al., 2007; Spassky et al., 2008). The primary cilium is a microtubule-based dynamic cellular appendage that is templated from the mother centriole. Both activation and repression of the Shh pathway are cilium dependent (Goetz and Anderson, 2010). Binding of Shh to Patched (Ptch1) triggers the removal of Ptch1 from cilia and promotes Smo enrichment in cilia, which mediates Gli transcriptional activator (GliA) formation. Germline heterozygous or conditional knockout of *Ptch1* or expression of the constitutively active *Smo* mutant *SmoM2* in NSCs or GC progenitors results in Shh-MBs (Goodrich et al., 1997; Schüller et al., 2008; Yang et al., 2008), whereas lack of cilia prevents *SmoM2*-induced medulloblastoma formation (Han et al., 2009).

In contrast, basal repression of Shh signaling involves protein kinase A (PKA)-mediated Gli repressor (GliR) formation in a cilium-dependent manner (Mukhopadhyay and Rohatgi, 2014). Lack of cilia promotes medulloblastoma formation upon expression of an active non-repressible form of Gli2, suggesting that the cilium-generated Gli3 repressor (Gli3R) restricts tumor progression (Han et al., 2009). Mutations in Suppressor of fused (*SUFU*), a negative regulator that functions by restraining cytoplasmic Gli3 and promoting Gli3R processing, have been reported in SHH-MBs (Taylor et al., 2002). However, early embryonic deletion of *Sufu* in the cerebellum did not exhibit tumorigenesis (Kim et al., 2011), whereas heterozygotes developed Shh-MBs only in a *p53*-null background (Lee et al., 2007). We recently identified the cilium-localized orphan G-protein-coupled receptor (GPCR) Gpr161 to be a negative regulator of Shh signaling during neural tube development (Mukhopadhyay et al., 2013). Gpr161 determines PKA-mediated Gli3R formation by constitutive cAMP signaling (Mukhopadhyay et al., 2013). Furthermore, the intraflagellar transport A (IFT-A) core complex and the tubby family protein Tulp3 coordinate Gpr161 trafficking to cilia (Badgandi et al., 2017), with either IFT-A or *Tulp3* mutants exhibiting high Shh signaling, unlike other mutants affecting cilia (Goetz and Anderson, 2010). Here we describe the role of Gpr161 in development of Shh-MBs by restricting premature and postnatal Shh signaling, ultimately limiting GC progenitor generation and proliferation.

RESULTS

Gpr161 Is Expressed in the Embryonic and Postnatal Cerebellum

Gpr161 was broadly expressed in the mouse cerebellum during late embryonic and postnatal development, as determined by radioisotopic *in situ* hybridization (Figure S1A) and qRT-PCR, respectively (Figure S1B). In particular, Gpr161 was highly expressed in the E15.5 cerebellar anlage, including the ventricular zone (VZ), uRL, and EGL (Figure S1A). Gpr161 also localized to the cilia of primary cultured GC progenitors (Figure S1C).

Gpr161 Deletion in Neural Stem Cells Induces Cerebellar Tumorigenesis

Gpr161 knockout mice are embryonic lethal by E10.5 (Mukhopadhyay et al., 2013). To conditionally delete *Gpr161*, we used a newly generated allele with loxP sites on either side of exon 4, which, upon recombination, results in a null allele (Hwang et al., 2017). We conditionally deleted *Gpr161* in mouse NSCs using *hGFAP-Cre* (Zhuo et al., 2001) (hereafter referred to as *GFAP-Gpr161* conditional knockout [cko]) (Figure 1A). Particularly in the cerebellar anlage, *hGFAP-Cre* can efficiently recombine genes in proliferating progenitors in the VZ and uRL that ultimately give rise to GC progenitors (Spassky et al., 2008). We confirmed that *Gpr161* was efficiently deleted from the cerebellum of *GFAP-Gpr161* cko mice using qRT-PCR (Figure 1B). Normally, GCs completely migrate out of the EGL into the IGL by postnatal day 16 (P16) (Corrales et al., 2004). However, even at P50, in *GFAP-Gpr161 cko* mice, we observed ectopic foci in the posterior cerebellum, constituting proliferating GC progenitors (based on Ki67 levels and bromodeoxyuridine [BrdU] incorporation in Pax6-positive GCs) (Figures S1D and S1F; Lin et al., 2001) and immature GC neurons (based on doublecortin immunostaining in Pax6-positive GCs) (Figures S1E and S1F). Strikingly, by 3–10 months, *GFAP-Gpr161* cko mice developed tumors in the cerebellum (Figures 1C and 1D). The tumors resembled histological features of human classic medulloblastoma, with solid sheets of tumor cells having uniform large nuclei and scant cytoplasm (Figures 1E and 1F). By 12 months, more than 50% of *GFAP-Gpr161* cko mice failed to survive (Figure 1G). As noted before for the ectopic foci, the tumors were positive for proliferating GC progenitors and immature GC neurons (Figures 1H–1O). Thus, *Gpr161* deletion in NSCs induces formation of cerebellar tumors.

(C) Representative picture showing brains of *GFAP-Gpr161* cko and WT mice (both 10 months old) after sectioning at the midline. Note the tumor (white dotted line) in the posterior cerebellum.

(D) H&E-stained sagittal sections showing tumors (white dotted lines) in the posterior cerebellum of *GFAP-Gpr161* cko mice (5–6 months old).

(E and F) H&E-stained section of tumor from *GFAP-Gpr161* cko mice (E) resembling that of human classic medulloblastoma (F).

(G) Kaplan-Meier survival curves of control (n = 19) and *GFAP-Gpr161* cko mice (n = 27). Data were collected when mice were found dead or mice were sick (hunched back and reduced mobility).

(H and I) Representative images of immunostaining for BrdU (upon 1-h pulse) (H) and Ki67/BrdU (I) in the cerebellum of 3- to 5-month-old mice.

(J and K) Quantification of $Ki67^+$ (J) or $BrdU^+$ (K) cells co-stained for DAPI per field of view. n = 3 fields/mice, 3 mice/genotype.

(L) qRT-PCR analysis of *Ki67* transcript levels in the *GFAP-Gpr161* cko tumors (n = 5) with respect to normal cerebellum from the WT (n = 6).

(M) $Pax6^+$ cells were present in the *GFAP-Gpr161* cko tumor but not in the WT molecular layer (ML).

(N and O) Representative images of doublecortin (DCX) immunostaining (N) and percentage of DCX^+ cells co-stained for DAPI per field of view (O) in the tumors of *GFAP-Gpr161* cko mice and cerebellum of the WT. n = 3 fields/mice, 3 mice/genotype, 3–5 months old.

Data represent mean ± SD. $^*p < 0.05$, $^{**}p < 0.01$ by log rank test (G) and Student's t test (B and J–L, and O). Scale bars indicate 2 mm (C), 1 mm (D, H, and N), and 100 μm (E, F, I, and M). (H) and (N) are tiled images. See also Figure S1.

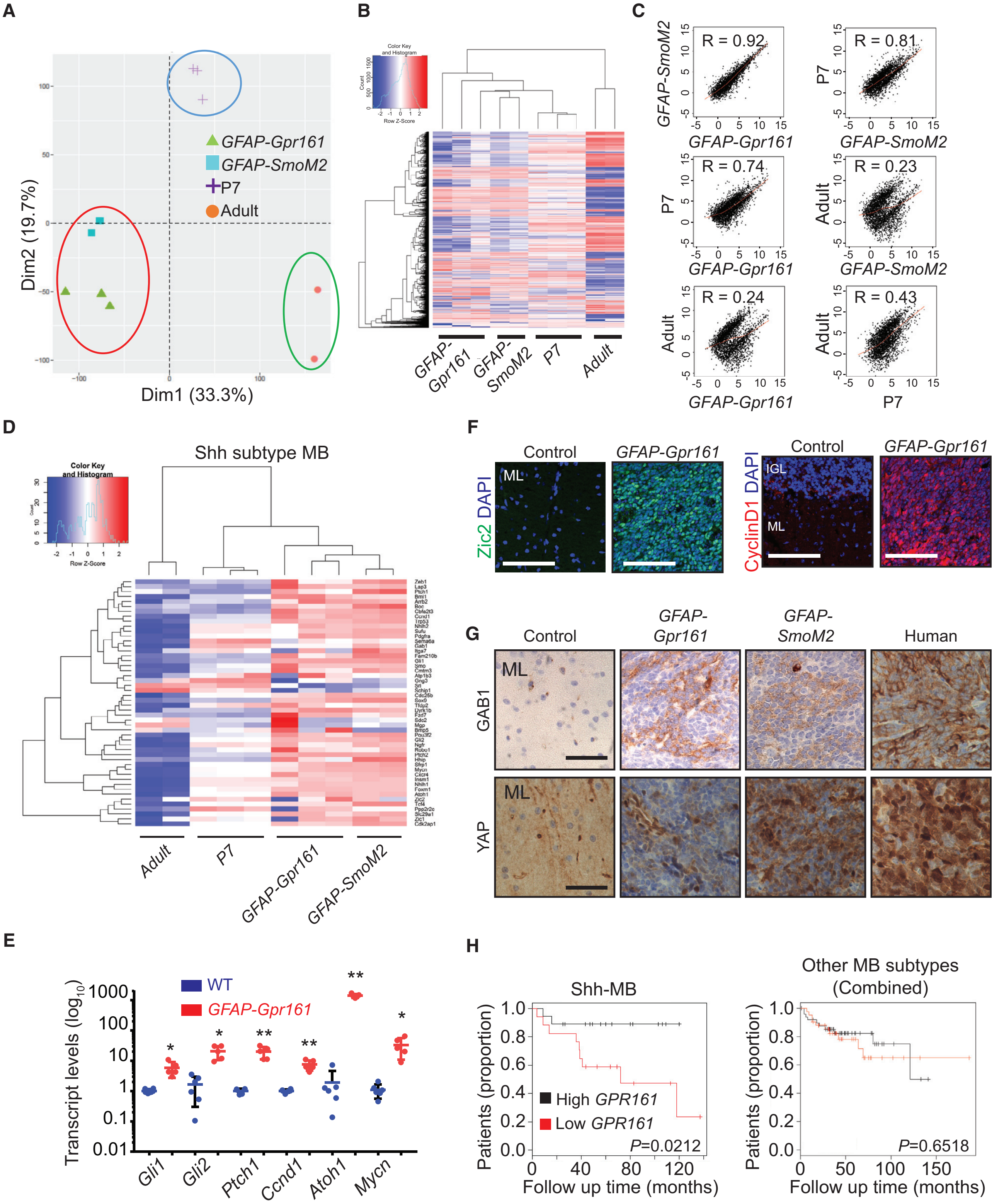

Figure 2. Gene Expression Profiles of Tumors Induced upon *Gpr161* Deletion Resemble Shh Subtype Medulloblastomas

(A and B) Principal-component analysis (PCA) (A) and hierarchical clustering analysis (B) of RNA-seq expression profiles of tumors from *GFAP-Gpr161* cko mice (3–5 months old, n = 3), Shh-MBs from *GFAP-SmoM2* mice (1 month old, n = 2), cerebellums of post-natal day 7 (P7, n = 3) mice, and adult mice (2 months old,

(legend continued on next page)

Gpr161 Deletion Induces Shh-MB Formation

Because Gpr161 is a basal suppressor of Shh signaling (Mukhopadhyay et al., 2013), we compared gene expression in *GFAP-Gpr161* cko tumors with a known model of Shh-MB generated by co-expressing a constitutively active Smo allele (*SmoM2(W539L)*^{EYFP}/+) (Jeong et al., 2004) with *hGFAP-Cre* (*GFAP-SmoM2*) and cerebellum from control P7 and adult mice. Principle-component analysis and hierarchical clustering of all transcripts demonstrated that *GFAP-Gpr161* cko tumors clustered with *hGFAP-SmoM2* tumors (Figures 2A and 2B), whereas regression analysis confirmed a direct correlation only between their transcription profiles (Figure 2C). Furthermore, the clustering analysis showed similarities between known Shh subtype-specific transcripts from these tumors (Figure 2D) but not with transcripts from other medulloblastoma subtypes (Figure S2A; Northcott et al., 2011). Expression of Shh signaling-specific transcripts such as *Gli1*, *Ptch1*, *CyclinD1* (*Ccnd1*), and *N-myc* (*Mycn*) and of the transcription factor *Gli2* in *GFAP-Gpr161* cko tumors was high with respect to control littermates by qRT-PCR (Figure 2E). Immunostaining showed increased CyclinD1 levels (Figure 2F) and high expression of other GC progenitor-specific markers, such as *Atoh1* (Figure 2E) and Zic2 (Aruga et al., 2002; Figure 2F), in the tumors. In addition, histological markers used in human SHH-MB diagnosis, such as GAB1 and YAP (Ellison et al., 2011), were highly expressed in *GFAP-Gpr161* cko and *GFAP-SmoM2* tumors, similar to human samples (Figure 2G). However, WNT subtype medulloblastoma-specific nuclear localization of β-catenin was absent (Figure S2B). In addition, *GFAP-Gpr161* cko medulloblastomas showed scattered neoplastic cells positive for the glial marker GFAP and neuronal differentiation by synaptophysin immunostaining resembling that of *GFAP-SmoM2* tumors and human Shh-MB samples (Figure S2B). Thus, *Gpr161* deletion in NSCs induces Shh-MB in mice, resembling the human SHH-MB subtype.

Low Expression of *GPR161* Correlates with Poor Prognosis in SHH-MB Patients

Mutations in the *Gpr161* locus were not seen in 300 sequenced tumors (Jones et al., 2012; Pugh et al., 2012; Robinson et al., 2012). In addition, we did not detect any homozygous deletions in the *Gpr161* locus in 827 patients tested (Northcott et al., 2017), implying that this locus is not a common hotspot for tumor initiation in patients. However, upon reevaluating the expression of *GPR161* from previously published expression data (Cho et al., 2011) with patient survival, we noted that the expression levels of *GPR161* tightly correlated with decreased patient survival length only in the SHH-MB subtype but not in other subtypes combined (Figures 2H and S2C). Thus, low *GPR161* is a prognostic indicator for survival in SHH-MB patients, implying that negative regulation of the SHH pathway might be critical for preventing tumor progression in humans.

Gpr161 Deletion in NSC or GC Progenitor-Specific Lineages Results in Shh-MB

Shh-MBs can be initiated in GC progenitors or NSCs, but tumorigenesis is associated with commitment to the GC lineage (Schüller et al., 2008; Yang et al., 2008). Multipotent NSCs expressing GFAP in the VZ give rise to Purkinje cells, Bergmann glia, astrocytes, and oligodendrocytes and also generate GC progenitors in the uRL (Schüller et al., 2008; Spassky et al., 2008; Yang et al., 2008). *hGFAP-Cre* starts expression in NSCs in the VZ by E12.5, followed by GC progenitors in the uRL (Spassky et al., 2008; Yang et al., 2008). In contrast, the *Nestin-Cre* line causes earlier and consistent expression in the entire neural tube by E11.5 (Blaess et al., 2008), whereas *Atoh1*-expressing GC progenitors appear in the embryonic uRL by E12.5 (Machold and Fishell, 2005; Wang et al., 2005). *Nestin-Cre; Gpr161*$^{fl/fl}$ and *Atoh1-Cre; Gpr161*$^{fl/fl}$ are hereafter referred to as *Nestin-Gpr161* cko and *Atoh1-Gpr161* cko, respectively. All three mouse models developed Shh-MBs (Figures 3A–3G). Although ∼50% *GFAP-Gpr161* cko mice developed Shh-MBs by 3 months or later (Figures 3C and 3E–3G), *Nestin-Gpr161* cko mice developed tumors by 2–8 months, and most were deceased by 8 months (Figures 3D and 3E–3G). Among the dying mice (n = 6), we observed a high tumor incidence upon histological examination (∼83%) (Figure 3F). *Atoh1-Gpr161* cko mice also developed tumors, but with much less severity and frequency. Only ∼20% of analyzed mice (n = 10) developed tumors by 4–6 months, and ∼6% died by 10 months of age (Figures 3B and 3E–3G). Because *Atoh1-Cre* results in GC progenitor-specific recombination, *Gpr161* deletion in GC progenitors is sufficient to induce tumorigenesis.

Similar to *GFAP-Gpr161* cko tumors, both *Nestin-Gpr161* and *Atoh1-Gpr161* cko tumors were GC-specific (Pax6-positive)

---

n = 2). The x and y axes in the PCA plot are first- and second-principal components, and the percentages shown on each axis refer to the percent of variance being explained by the corresponding principal components (Dim1 and Dim2). *GFAP-Gpr161* cko mice cluster with each other and are closely related to *GFAP-SmoM2* mice. The heatmap shows genes with an average expression level higher than 1 transcript per kilobase million (TPM) and variance of expression of more than 2 across all 10 samples.

(C) Regression analysis of RNA-seq data shows that tumors of *GFAP-Gpr161* cko mice and Shh subtype medulloblastoma of *GFAP-SmoM2* mice have a higher Pearson correlation coefficient (R) than other comparisons. The x and y axes show the log2-transformed TPM values.

(D) Heatmap and clustering analysis of Shh subtype-specific transcripts show that tumors of *GFAP-Gpr161* cko mice are similar to *GFAP-SmoM2* tumors.

(E) qRT-PCR analysis of transcript levels of Shh-MB candidate genes in tumors of *GFAP-Gpr161* cko mice (n = 6) compared with the WT cerebellums (n = 5).

(F) Tumors of *GFAP-Gpr161* cko mice (3–10 months old) expressed the GC marker Pax6 and the Shh pathway target CyclinD1 upon immunostaining and co-staining with DAPI.

(G) Immunohistochemical analysis confirms that tumors from *GFAP-Gpr161* cko mice exhibit an SHH subtype-specific staining pattern similar to mouse *GFAP-SmoM2* tumors and human SHH-MB (human).

(H) Poor survival specifically in SHH-MB patients with low *GPR161* expression in resected tumors (n = 52 in the SHH subtype and 135 in other subtypes combined). The top 50% and bottom 50% are considered high and low gene expression groups, respectively.

All data represent mean ± SD. Scale bars indicate (F) 100 μm and (G) 200 μm. $^{*}p < 0.05$, $^{**}p < 0.01$ by Student's t test or as shown using log rank test (H). IGL, internal granule layer; WT, littermate control (*Gpr161*$^{fl/fl}$ or *Gpr161*$^{fl/+}$). See also Figure S2.

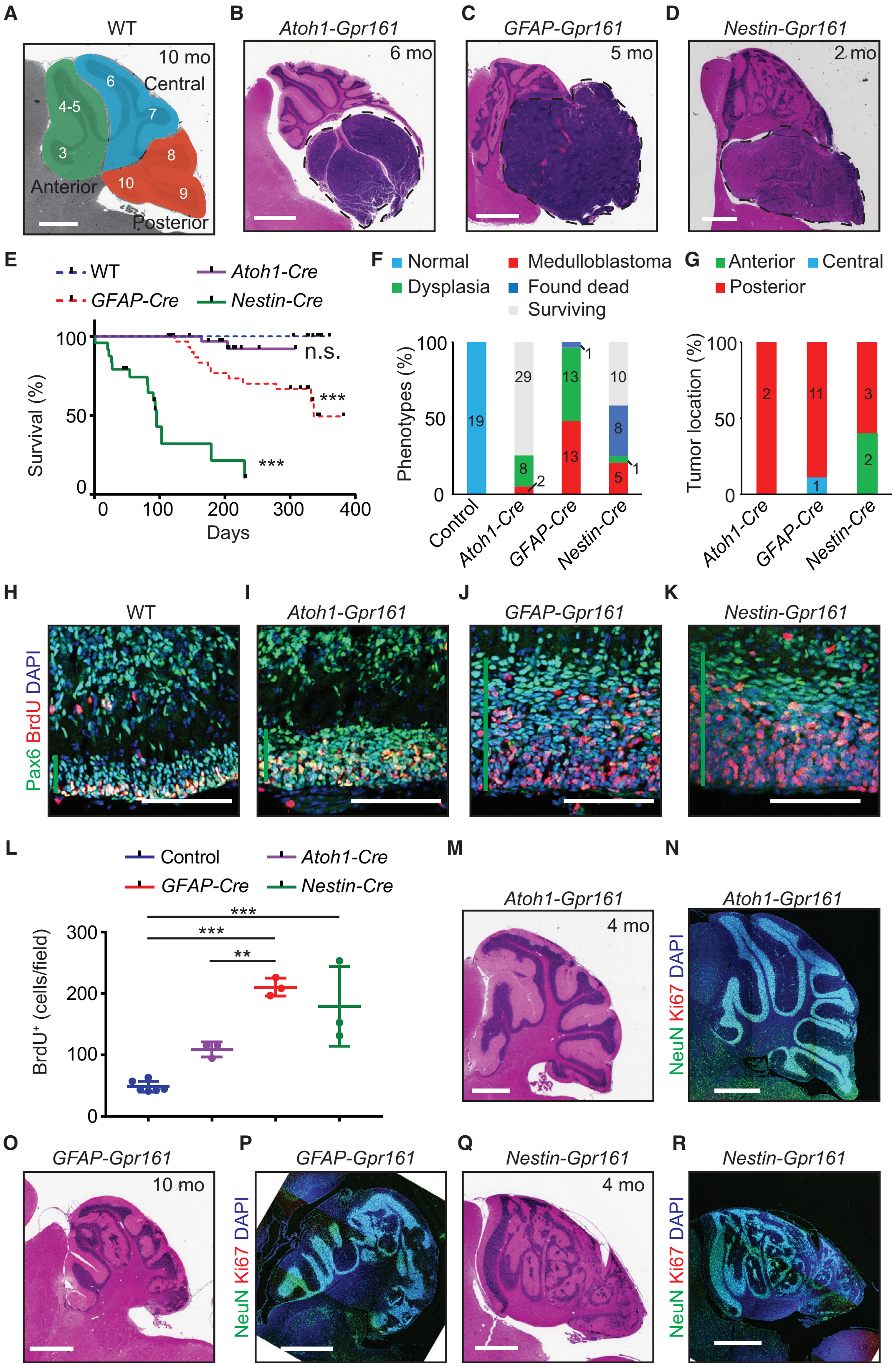

(legend on next page)

(Figure S3A) and resembled human classic medulloblastomas in histology (Figures 1F and S3B) and Shh-MBs by immunohistochemistry against GAB1 and YAP (Figures S3C–S3E). Interestingly, although tumors arising in *Atoh1-Gpr161* cko and *GFAP-Gpr161* cko predominantly affected posterior lobes, tumors in *Nestin-Gpr161* cko were also distributed anteriorly, possibly corresponding to the earlier depletion in NSCs (Figure 3G). All models were associated with an increase in thickness and proliferation of GC progenitors in the posterior EGL at P7 (Figures 3H–3L), suggesting increased proliferation postnatally. Overall, NSC-specific deletion causes more occurrences and a broader distribution of tumors and high mortality compared with GC progenitor-specific deletion.

Cerebellar Dysplasia and a Limited Number of Folia upon Loss of *Gpr161*

Irrespective of the development of tumors, we noticed abnormal cerebellar development (cerebellar dysplasia) resulting from mislocalized GCs during postnatal development (Figure 3F). The dysplastic regions were positive for the pan-neuronal marker NeuN and generally lacked proliferation (Figures 3M–3R), suggesting gradual regression into delayed neurogenesis starting from earlier proliferation (Figures 3H–3K). The dysplasia was strongest, earliest, and global in appearance in *Nestin-Gpr161* cko mice, followed by reduced severity in *GFAP-Gpr161* cko mice and only focal lesions in *Atoh1-Gpr161* cko mice (Figures 3M–3R). In addition, *Nestin-Gpr161* cko mice had a limited number of folia irrespective of developing tumors and/or dysplasia (Figures 3D and 3Q). Thus, *Gpr161* is critical for normal cerebellar development in addition to regulating tumorigenesis.

Temporal Progression of GC Progenitor Proliferation in *Nestin-Gpr161* cko Mice

To investigate tumorigenesis following *Gpr161* deletion, we further characterized the temporal progression of proliferative changes in GC progenitors. Deletion of *Gpr161* was confirmed by qRT-PCR in *Nestin-Gpr161* cko mice at P14 (Figure S4A). The thickness of the EGL was increased in *Nestin-Gpr161* cko mice compared with the littermate controls during postnatal development (Figures 4A–4G). The histological appearance of the proliferative cells in the outer EGL of *Nestin-Gpr161* cko mice showed gradual transformative changes with enlarged nuclei and a spindle-like appearance compared with the inner EGL (Figures 4A'–4F'). Shh pathway transcripts were highly upregulated in the cerebellum of *Nestin-Gpr161* cko mice compared with littermate controls at P14 by qRT-PCR (Figure 4H). Furthermore, radioisotopic RNA *in situ* hybridization demonstrated increased *Gli1* and *Ptch1* transcripts in the EGL of *Nestin-Gpr161* cko mice compared with littermate controls by P1 (Figure 4I). Proliferation of GC progenitors in the EGL was increased in *Nestin-Gpr161* cko mice compared with controls during postnatal development (Figures 4J and 4K and S4B). The inner EGL with P27-positive cells was also thickened, demonstrating that differentiation of GC progenitors was occurring in the EGL of *Nestin-Gpr161* cko mice. (Figures 4L and S4C). Increased proliferation of GC progenitors is associated with replication stress, accumulating DNA damage, and tumorigenesis (Mille et al., 2014), Interestingly, we observed increased DNA damage by γH2AX immunostaining in the posterior EGL of *Nestin-Gpr161* cko mice at P14 (Figures 4M and 4N and S4D) and in medulloblastomas of *GFAP-Gpr161* cko mice, indicating genomic instability (Figure S4E). Sox2 marks a rare quiescent stem cell population driving Shh-MB growth and relapse (Vanner et al., 2014). *GFAP-Gpr161* cko mouse tumors were also positive for Sox2, indicating accumulating cells with tumorigenic potential (Figure S4F). Thus, overproliferation of GC progenitors, accumulating DNA damage, and gradual transformative changes culminate into developing Shh-MB.

Dysplastic changes in *Nestin-Gpr161* cko mice were apparent from a gradual regression of proliferation into neurogenesis in non-tumor areas, except peripherally and in a few remaining pockets of small proliferative nests (Figures S4G and S4H). Similarly, there was a gradual regression of thickened EGL (P7) and cellular proliferation in the posterior lobe (1 month) (Figure S4I)

Figure 3. Loss of *Gpr161* in Either NSC or GC Progenitor-Specific Lineages Causes Shh-MB with Increased Incidence upon Earlier Depletion

(A–D) H&E-stained sagittal sections show (A) normal cerebellum in a WT ($Gpr161^{fl/fl}$ or $Gpr161^{fl/+}$) mouse and medulloblastoma in (B) *Atoh1-Gpr161* cko, (C) *GFAP-Gpr161* cko, and (D) *Nestin-Gpr161* cko mice at the designated ages. In (A), "anterior" indicates lobes 1–5, "central" indicates lobes 6 and 7, and "posterior" indicates lobes 8–10 (Legué et al., 2016).

(E) Kaplan-Meier survival curves of the WT (n = 19), *GFAP-Gpr161* cko mice (n = 27), *Atoh1-Gpr161* cko mice (n = 31), and *Nestin-Gpr161* cko mice (n = 24). Data of WT and *GFAP-Gpr161* cko mice (dotted line) from Figure 1G are shown for comparison.

(F) Histological analysis of the cerebellum in WT (10–12 months old, n = 19), *Nestin-Gpr161* cko mice (0–8 months old, n = 24; 6 dying mice were histologically analyzed at 2–8 months age; 9 of the 10 surviving mice were less than 93 days old during generation of the survival curve; E), *GFAP-Gpr161* cko mice (5–12 months, n = 27), and *Atoh1-Gpr161* cko mice (4–10 months old; n = 39; 8 histologically analyzed at 3–5 months age, 2 analyzed from dying animals at 5 and 7 months). Medulloblastoma, medulloblastoma with/without dysplasia; Dysplasia, misplaced granule neurons, both global and focal; Found dead, found dead with a disintegrated brain and excluded from histological analysis.

(G) Regional analysis of tumor location by H&E staining in different strains as follows: *Nestin-Gpr161* cko mice (3–8 months old, n = 5), *GFAP-Gpr161* cko mice (5–10 months old, n = 10), and *Atoh1-Gpr161* cko mice (5–7 months old; n = 2). Lobe designation is as in (A).

(H–K) Proliferating GC progenitors in the posterior (lobes 9 and 10) external granule layer (EGL) of cerebellums from (H) WT, (I) *Atoh1-Gpr161*, (J) *GFAP-Gpr161*, and (K) *Nestin-Gpr161* cko mice at P7. Vertical green lines mark the extent of the EGL.

(L) The number of $BrdU^+$ cells (upon 1-h pulse) was measured upon co-staining for DAPI cells per field of view. Three fields per mouse were analyzed. n = 3–6 mice/genotype.

(M–R) H&E-stained and $NeuN^+$-immunostained sagittal sections show global cerebellar dysplasia and/or focal ectopic granule neurons of (M and N) *Atoh1-Gpr161*, (O and P) *GFAP-Gpr161*, and (Q and R) *Nestin-Gpr161* cko mice at the designated ages. In (N), (P), and (R), $NeuN^+$ neurons are shown. Note that $Ki67^+$ cells were not observed.

Scale bars are 1 mm (A–D and M–R) and 100 μm (H–K). ***$p < 0.001$ by log rank test compared with the WT (E). n.s., not significant. **$p < 0.01$ by one-way ANOVA with Tukey's multiple comparisons test (L). Nuclei are stained by DAPI. (N), (P), and (R) are tiled images. See also Figure S3.

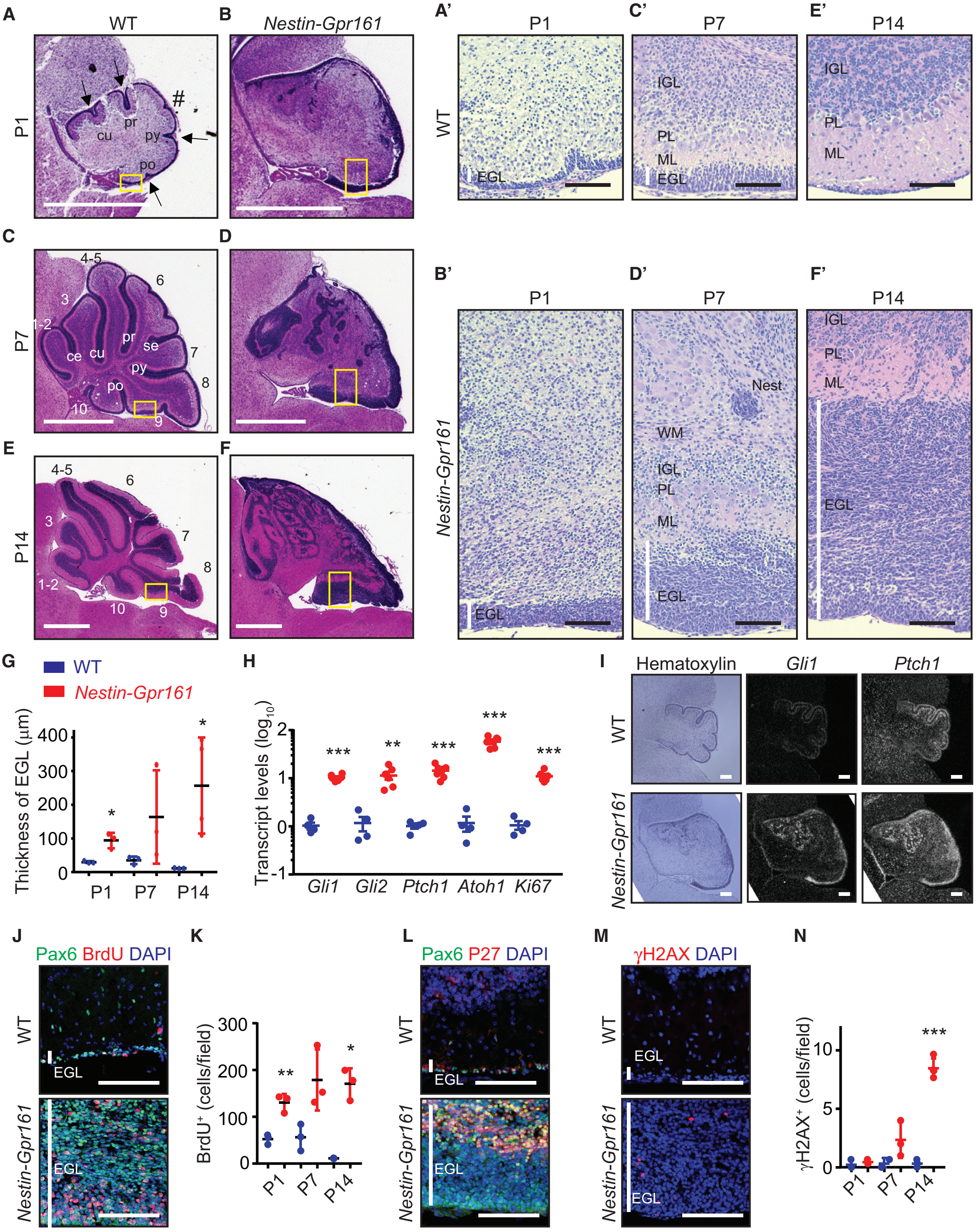

(legend on next page)

into focal dysplasia, irrespective of Shh-MB formation in *Atoh1-Gpr161* cko mice. A limited number of folia in *Nestin-Gpr161* cko was apparent as early as P0, with reduction of the principal fissures (Figures 4A–4F). Thus, *Gpr161* lacks results in a continuum of phenotypes, including tumorigenesis, dysplasia, and limited foliation.

Gpr161 Restricts Generation/Proliferation of GC Progenitors during Embryogenesis

Because deletion of *Gpr161* in earlier NSC-specific lineages caused more severe phenotypes than in GC progenitor-specific lineages, we systematically probed for developmental changes that accompany the generation of granule progenitors in the cerebellar anlage. In *Nestin-Gpr161* cko mice, we noted an increased size of the uRL and increased thickening of the formative EGL compared with littermate controls, starting as early as E14.5 and clearly evident by E16.5, suggesting that the areas where NSCs and GC progenitors locate are expanded in *Nestin-Gpr161* cko mice (Figures 5A–5D).

Most GC progenitors, including those derived from non-overlapping Atoh1- or Lmx1a-positive lineages, are Pax6-positive (Chizhikov et al., 2006; Lin et al., 2001; Millonig et al., 2000). Sox2 also marks a population of multipotent NSCs in the uRL and of GC progenitors in the formative EGL around E13.5 (Ahlfeld et al., 2013). In addition, a subpopulation of Pax6-positive progenitors in the uRL is also Olig2-positive. In agreement with increased thickness of the formative EGL, proliferating cells, Pax6-positive GC progenitors, as well as Sox2-positive NSCs were increased in the EGL of *Nestin-Gpr161* cko mice compared with littermate controls (Figures 5E-5G and S5A and S5B). Pax6-, Lmx1a-, and Olig2-positive GC progenitors along with Sox2-positive NSCs and proliferation in the uRL also increased in *Nestin-Gpr161* cko mice (Figures 5H–5M and S5C and S5D). Thus, Gpr161 restricts the generation and proliferation of GC progenitor and NSC pools in the EGL and uRL of the cerebellar anlage.

Premature Shh Signaling in GC Progenitors upon *Gpr161* Deletion

Next we determined mechanisms underlying Gpr161–mediated regulation of NSCs and GC progenitors in the cerebellar anlage. During embryogenesis, Shh is released from the hindbrain choroid plexus outside of the cerebellar anlage that promotes proliferation in the adjacent cerebellar VZ (Huang et al., 2010). BrdU incorporation (Figures S5E and S5F), Sox2-expressing radial glial progenitors (Figures S5G and S5H), Pax-2 expressing GABAergic interneuron progenitors (Figures S5I–S5J), and Shh pathway targets such as *Gli1* and *Ptch1* transcripts (Figure 5N) were increased in the cerebellar VZ of *Nestin-Gpr161* cko mice compared with littermate controls. Thus, Gpr161 restricts NSC pools in the VZ of the cerebellar anlage by inhibiting Shh signaling.

In contrast, inside the cerebellar anlage, Shh secretion by Purkinje neurons is not initiated until E18.5 (Corrales et al., 2004; Fuccillo et al., 2006; Huang et al., 2010; Kim et al., 2011; Lewis et al., 2004). Unexpectedly, we detected increased levels of Shh signaling targets (*Gli1* and *Ptch1* transcripts) and CyclinD1 in the EGL and outer uRL of *Nestin-Gpr161* cko mice compared with the littermate controls at E15.5 by *in situ* hybridization and immunofluorescence analysis (Figures 5N and 5O). Gli1 protein levels were also increased (Figure 5P). Importantly, Gli3R levels were significantly reduced in the cerebellar anlage of *Nestin-Gpr161* cko mice (Figure 5Q), concurrent with the role of Gpr161 in basal suppression of the Shh pathway by Gli3R processing prior to initiation of Shh-mediated morphogenetic signaling. Thus, Gpr161-mediated restriction of premature activation of the Shh pathway limits the GC progenitor pool during embryogenesis.

Overproliferation of GC Progenitors upon *Gpr161* Deletion Is Cilium Dependent

We next tested the role of cilia in phenotypes resulting from *Gpr161* deletion by combining it with deficiencies in the intraflagellar transport-B (IFT-B) complex protein *Ift88* that disrupts cilia (Haycraft et al., 2007). Thus, we generated single and double conditional knockouts of *Nestin-Cre*; *Ift88*$^{fl/fl}$ (*Nestin-Ift88* cko) and *Nestin-Cre*; *Gpr161*$^{fl/fl}$; *Ift88*$^{fl/fl}$ (*Nestin-Gpr161; Ift88* double conditional knockout [dko]), respectively. We first confirmed that *Gpr161* transcripts were reduced in *Nestin-Gpr161* cko and *Nestin-Gpr161; Ift88* dko mice (Figure 6A), whereas *Ift88* transcripts and Arl13b-positive primary cilia in P7 EGL were absent in *Nestin-Ift88* cko and *Nestin-Gpr161; Ift88* dko mice (Figures 6B and 6C). *Nestin-Ift88* cko mice had a smaller cerebellum with rudimentary folia compared with the littermate controls (Figure 6D). Strikingly, the cerebellums of *Nestin-Gpr161; Ift88* dko mice were smaller than those of *Nestin-Gpr161* cko mice and

Figure 4. GC Progenitor Proliferation and Dysplasia during Postnatal Development following *Gpr161* Deletion

(A–F) H&E-stained sagittal sections showing the thickened EGL, decreased foliation, and cerebellar dysplasia of *Nestin-Gpr161* cko mice (B, D, and F) compared with the WT (*Gpr161*$^{fl/fl}$ or *Gpr161*$^{fl/+}$) (A, C, and E) for P1 (A and B), P7 (C and D), and P14 (E and F). Arrows indicate fissures, and # indicates an expected fissure. Abbreviations for fissures: ce, precentral; cu, preculminate; pr, primary; se, secondary; py, pyramidal; po, posteriolateral.

(A'–F') High-magnification pictures of the yellow boxes in (A)–(F). White vertical lines indicate the EGL layer. PL, Purkinje/Bergmann glia layer; Nest, small proliferative nest (confirmed by BrdU staining); WM, white matter.

(G) The thickness of the EGL is increased in *Nestin-Gpr161* cko mice compared with littermate controls. n = 3–4 mice/genotype.

(H) qRT-PCR analysis shows increased Shh pathway transcripts in the cerebellums of *Nestin-Gpr161* cko mice compared with that of the WT at P14. n = 4–6 per genotype.

(I) Radioisotopic *in situ* hybridization shows increased *Gli1* and *Ptch1* transcript levels in the EGL of *Nestin-Gpr161* cko mice compared with littermate control mice at P1. Hematoxylin staining shows the morphology of the cerebellum.

(J–N) Temporal changes of (J and K) BrdU^{+} (1-h pulse) GC progenitors, (L) P27^{+} GC progenitors, and (M and N) γH2AX^{+} cells in the EGL of cerebellums of *Nestin-Gpr161* cko mice at P14. Note that data from Figure 3L at P7 are included in (K) for comparison. n = 3 mice/genotype.

All data represent mean ± SD. Scale bars indicate 1 mm (A–F), 100 μm (A'–F', J, L, and M), and 200 μm (I). $^{*}p < 0.05$, $^{**}p < 0.01$, and $^{***}p < 0.01$ by Student's t test. Nuclei are stained by DAPI. See also Figure S4.

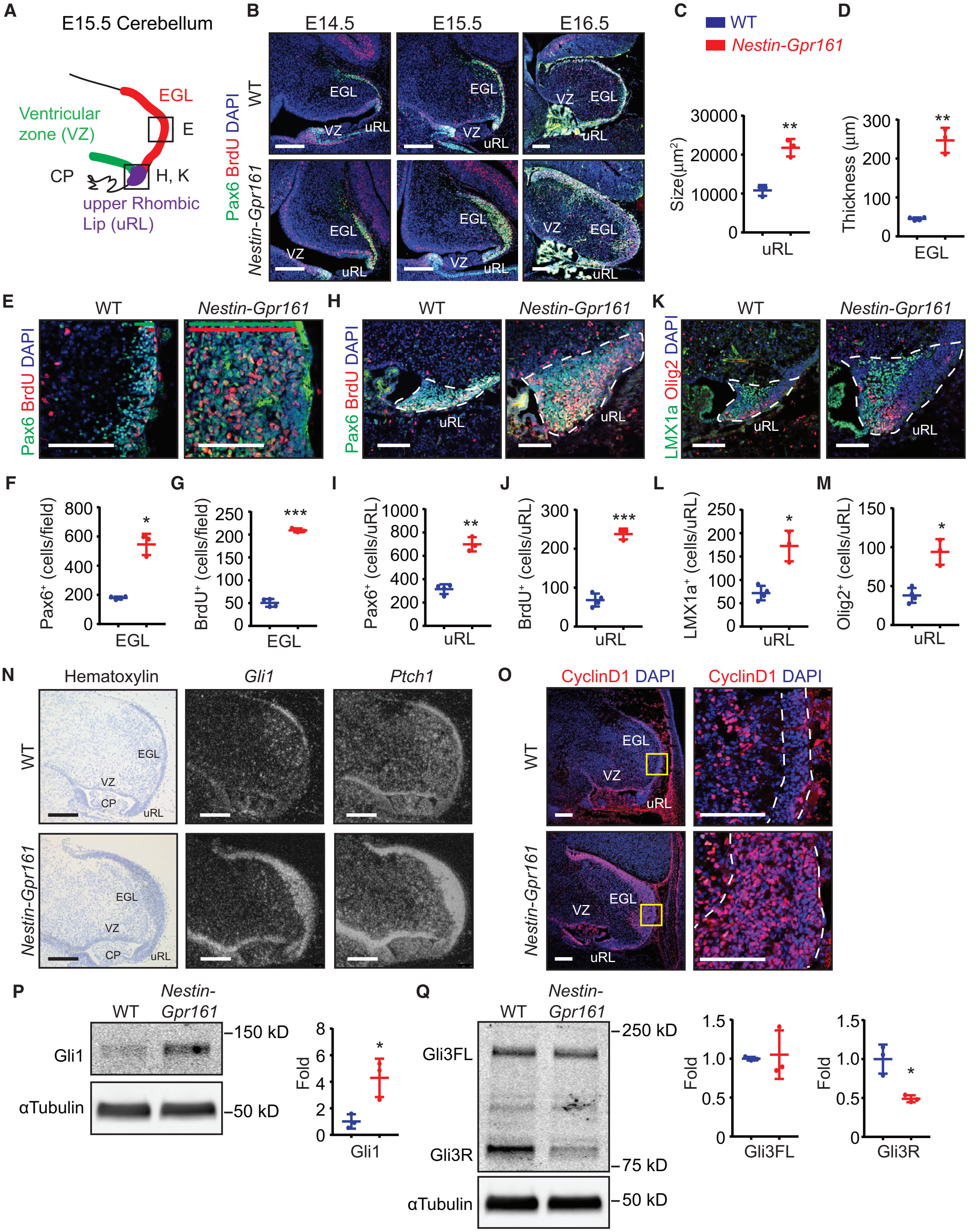

(legend on next page)

littermate controls at P7 but were almost indistinguishable from those of *Nestin-Ift88* cko mice (Figure 6D). The almost complete lack of EGL in *Nestin-Gpr161; Ift88* dko mice was similar to *Nestin-Ift88* cko mice (Figures 6E and 6G). In line with a lack of EGL, Pax6-positive GC progenitors, BrdU-positive proliferation, and the Shh pathway targets *Gli1* and *Ptch1* were drastically decreased in *Nestin-Gpr161; Ift88* dko and *Nestin-Ift88* cko mice compared with either WT or *Nestin-Gpr161* cko mice (Figures 6F and 6H–6J). Thus, primary cilia are required for normal proliferation and overproliferation of GC progenitors caused by *Gpr161* deletion in the postnatal cerebellum.

Lack of Cilia Prevents Premature Shh Signaling and Excessive Generation of GC Progenitors upon *Gpr161* Deletion during Embryogenesis

We next examined whether excessive generation and proliferation of GC progenitors during embryogenesis upon lack of *Gpr161* are also dependent on cilia at E15.5. Pax6-expressing GC progenitors were ciliated at this stage in the cerebellar anlage (Figure S6A), and cilia were absent upon *Nestin-Cre*-mediated conditional deletion of *Ift88* (Figure 7A). The number and proliferation of GC progenitors in the formative EGL and uRL of *Nestin-Ift88* cko mice that lack cilia were similar to littermate controls (Figures 7B–7F and S6B–S6D). In contrast, the thickness of the EGL and the number and proliferation of GC progenitors in the EGL and uRL in *Nestin-Gpr161* cko mice were increased compared with the littermate controls (Figures 7B–7F; Figure S6B–S6D). The thickness of the EGL and the number and proliferation of GC progenitors in *Nestin-Gpr161; Ift88* dko mice were decreased compared with *Nestin-Gpr161* cko mice and similar to littermate controls or *Nestin-Ift88* cko mice (Figures 7B–7F and S6B–S6D). The Shh pathway target CyclinD1 was significantly high in *Nestin-Gpr161* cko mice compared with *Nestin-Gpr161; Ift88* dko mice, which were similar to littermate controls or *Nestin-Ift88* cko mice (Figure 7G and S6E). Thus, the presence of cilia prevents excessive generation and proliferation of GC progenitors during embryogenesis by Gpr161-mediated repression of the Shh pathway but has no effect on normal progenitor development during embryogenesis.

DISCUSSION

Gpr161 Is a *Bona Fide* Tumor Suppressor in Shh-MB Formation

Here we establish *Gpr161* as a *bona fide* tumor suppressor in Shh-MB. Multiple lines of evidence, including RNA sequencing (RNA-seq) analysis and immunohistochemistry, group the Shh-MB tumors in *Gpr161* conditional knockout mice with *SmoM2*-induced tumors in mice and human SHH-MB. To our knowledge, this is the only rhodopsin family GPCR to be implicated in medulloblastoma pathogenesis. We also note that lower levels of *GPR161* transcript correlate with tumor progression in SHH-MB patients but not in other subtypes. Thus, *GPR161* levels might also play a role in the progression of human SHH-MB tumors and be useful as a prognostic biomarker. The severity and extent of tumorigenesis is weaker than with respect to *Ptch1* conditional knockout mice (Yang et al., 2008) because Shh pathway induction upon *Gpr161* depletion is weaker than upon Smo activation (Mukhopadhyay et al., 2013). Nonetheless, the natural progression of tumorigenesis upon *Gpr161* deletion instructs on stages of Shh-MB formation, such as increased generation and proliferation of GC progenitors leading gradually to tumorigenesis or dysplasia (Figure 7H). As opposed to Gpr161's role as a tumor suppressor in Shh-MB, *GPR161* levels are elevated in triple-negative breast cancer, with *GPR161* overexpression promoting proliferation and invasiveness in mammary epithelial cells by Shh-independent mechanisms (Feigin et al., 2014).

Gpr161 Regulates GC Progenitor Proliferation in a Cilium-Dependent Manner

Lack of *Ift88* prevented both basal and *Gpr161* deletion-induced excessive postnatal GC proliferation and Shh-mediated signaling. Ift88 is known to play other roles in the cell cycle in addition to IFT in cilia (Delaval et al., 2011). Deletion of the anterograde

Figure 5. Gpr161 Limits Premature Shh Signaling in GC Progenitors during Embryogenesis

(A) A cartoon of the cerebellar anlage at E15.5. EGL, formative external granule layer; uRL, upper rhombic lip; VZ, ventricular zone; CP, hindbrain choroid plexus.

(B) $Pax6^+$- and $BrdU^+$-stained sagittal sections show gradual thickening of the formative EGL at different embryonic stages in *Nestin-Gpr161* cko mice.

(C and D) Increased area of the uRL (C) and thickened formative EGL (D) are shown in *Nestin-Gpr161* cko mice (n = 3) compared with WT mice (n = 4) at E16.5.

(E–G) Representative images of proliferating GC progenitors in the formative EGL at E16.5 of *Nestin-Gpr161* cko mice (n = 3) and WT mice (n = 4) (E). The location of the EGL region depicted is indicated in the black box in (A). The extent of the EGL ($Pax6^+$) and $BrdU^+$ proliferating cells is shown using a green and red bar, respectively. The numbers of (F) $Pax6^+$ GC progenitors and (G) $BrdU^+$ (1 h incorporation) proliferating cells are increased in the EGL regions of *Nestin-Gpr161* cko mice compared with that of the WT at E16.5.

(H–J) Representative pictures of $Pax6^+$ GC progenitors and $BrdU^+$ proliferating cells in the uRL of E16.5 *Nestin-Gpr161* cko mice and WT mice (H). The location is indicated in the black box in (A). The numbers of (I) $Pax6^+$ GC progenitor cells and (J) $BrdU^+$ proliferating cells are increased in the uRL of *Nestin-Gpr161* mice (n = 3) compared with the WT (n = 4) at E16.5.

(K–M) Representative pictures of $Lmx1a^+$ and $Olig2^+$ cells in the uRL of E16.5 *Nestin-Gpr161* cko mice (n = 3) and WT mice (n = 4) (K). The location is indicated in the black box in (A). The numbers of (L) $Lmx1a^+$ and (M) $Olig2^+$ cells are increased in the uRL of *Nestin-Gpr161* cko mice compared with that of the WT at E16.5.

(N) Radioisotopic *in situ* hybridization showed increased *Gli1* and *Ptch1* transcript levels in the formative EGL, outer uRL, and VZ of *Nestin-Gpr161* cko mice compared with WT mice at E15.5. Hematoxylin staining shows the morphology of the cerebellum.

(O) Representative images of $CyclinD1^+$ cells in the cerebellum of E15.5 *Nestin-Gpr161* cko mice and littermate control mice. The EGL is marked by white dotted lines.

(P and Q) Immunoblotting for Gli1 (P) and Gli3 (Q) and quantification (after normalization with α-tubulin levels) in E15.5 cerebellar anlagen of control littermates and *Nestin-Gpr161* cko mice (n = 3 each). High Gli1 levels and low Gli3R levels are seen in *Nestin-Gpr161* cko mice. Gli3FL, Gli3 full-length; Gli3R, Gli3 repressor. All data represent mean ± SD. Scale bars indicate 200 μm (B, N, and O, left) and 100 μm (E, H, K, and O, insets). Nuclei are stained by DAPI. *$p < 0.05$, **$p < 0.01$, ***$p < 0.001$ by Student's t test. WT, littermate control (*Nestin-Cre; Gpr161*$^{fl/+}$ or *Gpr161*$^{fl/fl}$ or *Gpr161*$^{fl/+}$). (B) is a tiled image. See also Figure S5.

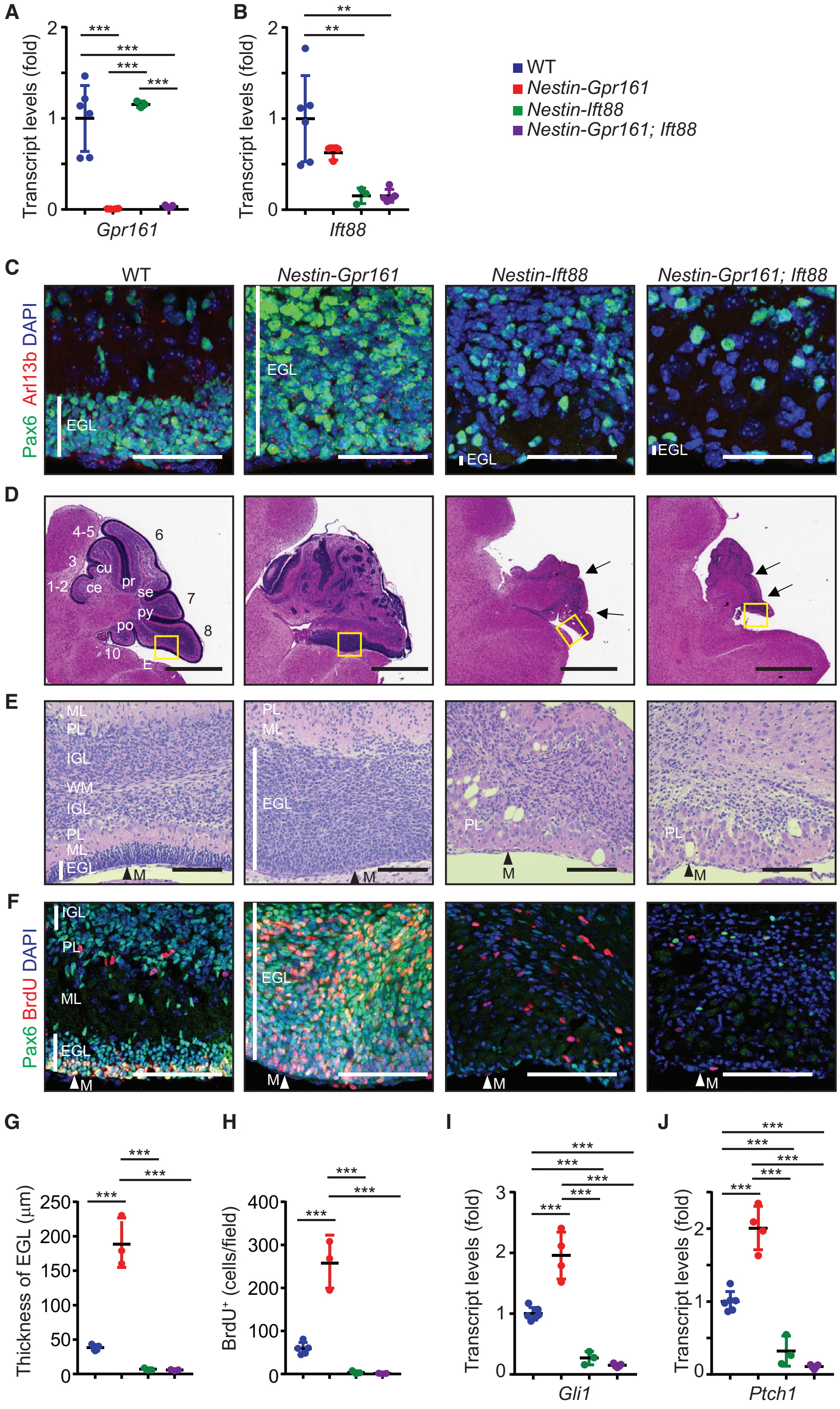

(legend on next page)

IFT kinesin II subunit *Kif3a* using *hGFAP-Cre* also disrupts cilia in GC progenitors and reduces proliferation in the postnatal EGL (Spassky et al., 2008). Because conditional knockouts of *Ift88* phenocopy *Kif3a* mutants in preventing GC progenitor proliferation postnatally, lack of cilia in *Ift88* mutants likely accounts for EGL deficiency in single or double mutants with *Gpr161*. Overall, Gpr161-mediated negative regulation through cilia functions as a rheostat in fine-tuning Shh-dependent signaling during postnatal GC progenitor proliferation (Figure 7H).

Restriction of Premature Shh Signaling in the Cerebellar Anlage by Gpr161 in a Cilium-Dependent Manner

Gpr161 deletion during embryogenesis promotes prematurely high downstream activity of the Shh pathway from lack of Gli3R formation, causing increased GC progenitor proliferation in the cerebellar anlage in the absence of Shh. Furthermore, we detect a general increase in cellularity in the uRL, along with an increase in Pax6-, Lmx1a-, and Olig2-positive GC progenitors and Sox2-positive NSCs. Interestingly, only excessive generation and overproliferation of GC progenitors during embryogenesis from *Gpr161* deletion were cilium dependent, unlike baseline production of GC progenitors. Thus, Gli3R-mediated suppression of premature Shh signaling through cilia critically determines balanced generation of GC progenitors in the uRL and proliferation of GC progenitors in the formative EGL (Figure 7H). The low Shh signaling compartment in the cerebellar anlage might be necessary to restrict generation of GC progenitor pools in the uRL, prevent undue proliferation of GC progenitors during migration into the formative EGL, and limit excessive proliferation in the formative EGL before initiation of foliation. Restricting premature Shh pathway activity in the cerebellar anlage exemplifies a broader role of suppression of downstream signaling in the absence of Shh in developmental (Hwang et al., 2017) and tumor initiation pathways.

EXPERIMENTAL PROCEDURES

Mice

All the animals in the study were handled according to protocols approved by the University of Texas (UT) Southwestern Institutional Animal Care and Use Committee, and the mouse colonies were maintained in a barrier facility at UT Southwestern, in agreement with the State of Texas legal and ethical standards of animal care. The newly generated *Gpr161* floxed mouse strain was maintained in a C57BL/6 background (Hwang et al., 2017). *Nestin-Cre* mice (B6.Cg-Tg(Nes-cre)1Kln/J, stock no. 003771), *Atoh1-Cre* mice (B6.Cg-Tg(Atoh1-cre)1Bfri/J, stock no. 011104), *hGFAP-Cre* mice (FVB-Tg(GFAP-cre)25Mes/J, stock no. 004600), *SmoM2* mice (*Gt(ROSA)26Sor*$^{tm1(Smo/EYFP)Amc}$/J, stock no. 005130), and *Ift88*$^{fl/fl}$ (*B6.129P2-Ift88*^{tm1Bky}/J, stock no. 022409) mice were obtained from Jackson Laboratory (Bar Harbor, ME). Both male and female mice were analyzed in all experiments. We did not notice any difference between wild-type or heterozygous animals for both *Gpr161* and *Ift88* floxed alleles with or without *Cre* recombinase, and, thus, all were included as littermate controls, as mentioned in the respective figure legends. Noon of the day on which a vaginal plug was found was considered E0.5. Tail DNAs were used for genotyping embryos. Genotyping details are provided in the Supplemental Experimental Procedures.

Patient Survival Analysis

Published patient data were re-analyzed for survival and gene expression levels (Cho et al., 2011), and the top 50% and bottom 50% gene expression groups were considered high and low gene expression groups, respectively. The relationship between mRNA expression and survival time was analyzed according to the Kaplan-Meier method using log rank statistics. Survival plots were generated with R studio. The p values were calculated by log-rank tests.

Cell Quantification and Statistics

For EGL, uRL, and VZ quantification from a "field" (Figures 3, 4, 5, 6, and 7 and S5 and S6), we averaged marker-positive cells from three images of different sections of the designated region from each mouse embryo or pup taken with a 40× objective in an LSM780. For the uRL quantification in Figure 5, we averaged marker-positive cells in the uRL from three images of different sections of the designated region from each embryo taken with 20× objective in an LSM780. Data from 3–11 mice per genotype are shown. The thickness of the EGL layer was measured manually using ImageJ from at least three sections per mouse. No blinding was performed. Sample sizes were based on our experience with these assays. All data in the figures are expressed as mean ± SD. To assess the statistical significance of differences among treatments, we often performed unpaired, two-sided Student's t tests that assumed unequal variances in treatments, one-way ANOVA with Sidak's multiple comparisons tests, one-way ANOVA with Turkey multiple comparisons tests, and log rank tests. No mice or samples were excluded from any experiments, except for Figure 3F (because degraded brains were not amenable to analysis). Microsoft Excel and GraphPad Prism (GraphPad, La Jolla, CA) were used for statistical analysis. Values of $p < 0.05$ were considered significant. Analysis of RNA-seq data is described in the Supplemental Experimental Procedures.

DATA AND SOFTWARE AVAILABILITY

The accession number for the RNA-seq data reported in this paper is SRA: SRP114953.

Figure 6. Gpr161 Prevents GC Progenitor Proliferation in a Cilium-Dependent Manner

(A and B) Gpr161 (A) and *Ift88* (B) transcript levels in P7 cerebellums of WT, *Nestin-Gpr161* cko, *Nestin-Ift88* cko, and *Nestin-Gpr161*; *Ift88* dko mice. n = 3-6 mice per genotype.

(C) Representative pictures of Arl13b$^+$ primary cilia in Pax6$^+$ GC progenitors in the EGL in the cerebellum of WT, *Nestin-Gpr161* cko, *Nestin-Ift88* cko, and *Nestin-Gpr161*; *Ift88* dko mice at P7. Note that Arl13b$^+$ primary cilia are not observed in the rudimentary EGL of *Nestin-Ift88* cko and *Nestin-Gpr161*; *Ift88* dko mice.

(D and E) H&E-stained sagittal sections of the corresponding insets in (D) as depicted in (E) shows increased thickness of the EGL in *Nestin-Gpr161* cko mice and almost nonexistent EGL and partial foliation in *Nestin-Ift88* cko mice and *Nestin-Gpr161*; *Ift88* dko mice at P7. Arrows point to rudimentary fissures.

(F) Representative pictures of Pax6$^+$ GC progenitors and BrdU$^+$ proliferating cells in the EGL at P7. Vertical white lines denote extent of EGL (C, E, and F). M, meninges (E and F).

(G) Thickness of the EGL of P7 cerebellum. n = 3–6 mice per genotype.

(H) Number of BrdU$^+$ cells (upon 1-h pulse) measured in the EGL of P7 cerebellums of the designated genotypes. n = 3–6 mice/genotype.

(I and J) qRT-PCR analysis shows increased Shh pathway transcripts, *Gli1* (I) and *Ptch1* (J), in the cerebellums of *Nestin-Gpr161* cko mice compared with that of WT and *Nestin-Gpr161*; *Ift88* dko mice at P7. n = 3–6 mice/genotype.

Scale bars indicate (C) 50 μm, (D) 1 mm, and (E and F) 100 μm. Nuclei are stained by DAPI. $^{**}p < 0.01$, $^{***}p < 0.001$ by one-way ANOVA with Tukey's multiple comparisons test. *Nestin-Gpr161* cko is *Nestin-Cre; Gpr161*$^{fl/fl}$*; Ift88*$^{fl/+}$; *Nestin-Ift88* cko is *Nestin-Cre; Ift88*$^{fl/fl}$*; Gpr161*$^{fl/+}$; *Nestin-Gpr161; Ift88* dko is *Nestin-Cre; Gpr161*$^{fl/fl;}$ *Ift88*$^{fl/fl}$; WT is littermate control (*Nestin-Cre; Gpr161*$^{fl/+}$*; Ift88*$^{fl/+}$ or *Gpr161*$^{fl/fl}$*; Ift88*$^{fl/fl}$ or *Gpr161*$^{fl/+}$*; Ift88*$^{fl/fl}$ or *Gpr161*$^{fl/fl}$*; Ift88*$^{fl/+}$). The other abbreviations are as in Figures 4 and 5.

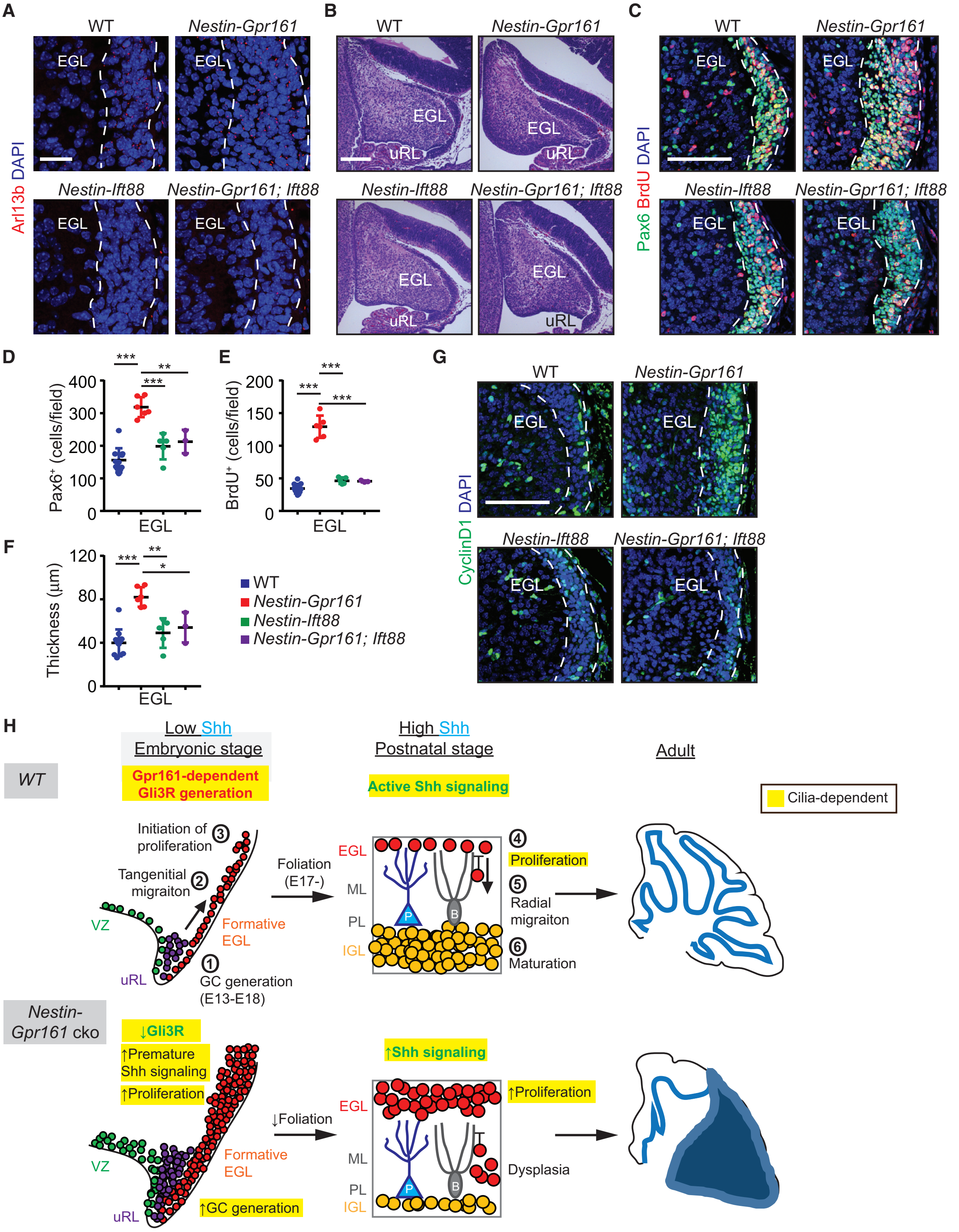

(legend on next page)

SUPPLEMENTAL INFORMATION

Supplemental information includes Supplemental Experimental Procedures and six figures and can be found with this article online at https://doi.org/10.1016/j.celrep.2018.01.018.

ACKNOWLEDGMENTS

This work was supported by a recruitment grant from the Cancer Prevention and Research Institute of Texas (R1220 to S.M.), an A-grant from the Alex's Lemonade Foundation (to S.M.), and an R01 grant from the NIH (1R01GM113023-01 to S.M.). We thank Dr. Stephen Brown at University of Vermont for the Zic2 antibody. We thank Victor Santana for technical support with histology. We thank Dr. Robert Hammer and the Mouse Transgenic Core, Live Cell Imaging Facility (NIH S10RR029731), Bioinformatic Core (Cancer Prevention and Research Institute of Texas RP150596), and the Molecular Pathology Core at UT Southwestern Medical Center.

AUTHOR CONTRIBUTIONS

I.S.S. and S.M. conceived the project, designed the experiments, analyzed most of the data, and wrote the paper. I.S.S. performed most of the experiments. S.-H.H. generated $Gpr161^{fl/fl}$ mice and assisted with *in situ* hybridization experiments. B.N.S. performed the *Gpr161* expression analysis and assisted with preliminary characterization of *GFAP-Gpr161* cko mice. X.W., P.S., and M.D.T. performed human patient data analysis. J.K., M.K., and Z.X. analyzed RNA-seq data. J.M.S. performed the radiometric *in situ* hybridization experiments. V.R. provided human tumor samples and served as a consultant pathologist for tumor diagnosis and immunohistochemistry interpretation.

DECLARATION OF INTERESTS

The authors declare no competing interests.

Received: November 21, 2017
Revised: January 2, 2018
Accepted: January 5, 2018
Published: January 30, 2018

REFERENCES

Ahlfeld, J., Favaro, R., Pagella, P., Kretzschmar, H.A., Nicolis, S., and Schüller, U. (2013). Sox2 requirement in sonic hedgehog-associated medulloblastoma. Cancer Res. *73*, 3796–3807.

Aruga, J., Inoue, T., Hoshino, J., and Mikoshiba, K. (2002). Zic2 controls cerebellar development in cooperation with Zic1. J. Neurosci. *22*, 218–225.

Badgandi, H.B., Hwang, S.H., Shimada, I.S., Loriot, E., and Mukhopadhyay, S. (2017). Tubby family proteins are adapters for ciliary trafficking of integral membrane proteins. J. Cell Biol. *216*, 743–760.

Blaess, S., Stephen, D., and Joyner, A.L. (2008). Gli3 coordinates three-dimensional patterning and growth of the tectum and cerebellum by integrating Shh and Fgf8 signaling. Development *135*, 2093–2103.

Chizhikov, V.V., Lindgren, A.G., Currle, D.S., Rose, M.F., Monuki, E.S., and Millen, K.J. (2006). The roof plate regulates cerebellar cell-type specification and proliferation. Development *133*, 2793–2804.

Chizhikov, V.V., Davenport, J., Zhang, Q., Shih, E.K., Cabello, O.A., Fuchs, J.L., Yoder, B.K., and Millen, K.J. (2007). Cilia proteins control cerebellar morphogenesis by promoting expansion of the granule progenitor pool. J. Neurosci. *27*, 9780–9789.

Cho, Y.J., Tsherniak, A., Tamayo, P., Santagata, S., Ligon, A., Greulich, H., Berhoukim, R., Amani, V., Goumnerova, L., Eberhart, C.G., et al. (2011). Integrative genomic analysis of medulloblastoma identifies a molecular subgroup that drives poor clinical outcome. J. Clin. Oncol. *29*, 1424–1430.

Corrales, J.D., Rocco, G.L., Blaess, S., Guo, Q., and Joyner, A.L. (2004). Spatial pattern of sonic hedgehog signaling through Gli genes during cerebellum development. Development *131*, 5581–5590.

Dahmane, N., and Ruiz i Altaba, A. (1999). Sonic hedgehog regulates the growth and patterning of the cerebellum. Development *126*, 3089–3100.

Delaval, B., Bright, A., Lawson, N.D., and Doxsey, S. (2011). The cilia protein IFT88 is required for spindle orientation in mitosis. Nat. Cell Biol. *13*, 461–468.

Ellison, D.W., Dalton, J., Kocak, M., Nicholson, S.L., Fraga, C., Neale, G., Kenney, A.M., Brat, D.J., Perry, A., Yong, W.H., et al. (2011). Medulloblastoma: clinicopathological correlates of SHH, WNT, and non-SHH/WNT molecular subgroups. Acta Neuropathol. *121*, 381–396.

Feigin, M.E., Xue, B., Hammell, M.C., and Muthuswamy, S.K. (2014). G-protein-coupled receptor GPR161 is overexpressed in breast cancer and is a promoter of cell proliferation and invasion. Proc. Natl. Acad. Sci. USA *111*, 4191–4196.

Fuccillo, M., Joyner, A.L., and Fishell, G. (2006). Morphogen to mitogen: the multiple roles of hedgehog signalling in vertebrate neural development. Nat. Rev. Neurosci. *7*, 772–783.

Goetz, S.C., and Anderson, K.V. (2010). The primary cilium: a signalling centre during vertebrate development. Nat. Rev. Genet. *11*, 331–344.

Goodrich, L.V., Milenković, L., Higgins, K.M., and Scott, M.P. (1997). Altered neural cell fates and medulloblastoma in mouse patched mutants. Science *277*, 1109–1113.

Han, Y.G., Kim, H.J., Dlugosz, A.A., Ellison, D.W., Gilbertson, R.J., and Alvarez-Buylla, A. (2009). Dual and opposing roles of primary cilia in medulloblastoma development. Nat. Med. *15*, 1062–1065.

Haycraft, C.J., Zhang, Q., Song, B., Jackson, W.S., Detloff, P.J., Serra, R., and Yoder, B.K. (2007). Intraflagellar transport is essential for endochondral bone formation. Development *134*, 307–316.

Herculano-Houzel, S. (2009). The human brain in numbers: a linearly scaled-up primate brain. Front. Hum. Neurosci. *3*, 31.

Huang, X., Liu, J., Ketova, T., Fleming, J.T., Grover, V.K., Cooper, M.K., Litingtung, Y., and Chiang, C. (2010). Transventricular delivery of Sonic hedgehog is essential to cerebellar ventricular zone development. Proc. Natl. Acad. Sci. USA *107*, 8422–8427.

Hwang, S.H., White, K.A., Somatilaka, B.N., Shelton, J.M., Richardson, J.A., and Mukhopadhyay, S. (2017). The G-protein-coupled receptor Gpr161 regulates forelimb formation, limb patterning and skeletal morphogenesis in a primary cilium-dependent manner. Development *145*, dev.154054.

Jeong, J., Mao, J., Tenzen, T., Kottmann, A.H., and McMahon, A.P. (2004). Hedgehog signaling in the neural crest cells regulates the patterning and growth of facial primordia. Genes Dev. *18*, 937–951.

Figure 7. Gpr161 Prevents Premature Shh Signaling during Embryogenesis in a Cilium-Dependent Manner

(A) Arl13b$^+$ primary cilia in the formative EGL (white dashed line) at E15.5.

(B) H&E-stained sagittal sections of the embryonic cerebellum at E15.5.

(C–F) Representative images of proliferating GC progenitors in the formative EGL at E15.5 (C) and quantification (D and E). Also shown is the thicknesses of the EGL at E15.5 (F). The numbers of mice were as follows: WT (n = 11), *Nestin-Gpr161* cko (n = 6), *Nestin-Ift88* cko (n = 5), and *Nestin-Gpr161;Ift88* dko (n = 3).

(G) Increased number of Cyclin D1$^+$ cells in the formative EGL of *Nestin-Gpr161* cko mice at E15.5.

(H) Cartoon summarizing the role of *Gpr161* in cerebellar development and Shh-MB pathogenesis. See Discussion for details.

Scale bars indicate (A and B) 200 μm and (C and G) 100 μm. Nuclei are stained by DAPI. $^{*}p < 0.05$, $^{**}p < 0.01$, $^{***}p < 0.001$ by one-way ANOVA with Sidak multiple comparisons test. Abbreviations of genotypes are as in Figure 6. See also Figure S6.

Jones, D.T., Jäger, N., Kool, M., Zichner, T., Hutter, B., Sultan, M., Cho, Y.J., Pugh, T.J., Hovestadt, V., Stütz, A.M., et al. (2012). Dissecting the genomic complexity underlying medulloblastoma. Nature *488*, 100–105.

Kim, J.J., Gill, P.S., Rotin, L., van Eede, M., Henkelman, R.M., Hui, C.C., and Rosenblum, N.D. (2011). Suppressor of fused controls mid-hindbrain patterning and cerebellar morphogenesis via GLI3 repressor. J. Neurosci. *31*, 1825–1836.

Lee, Y., Kawagoe, R., Sasai, K., Li, Y., Russell, H.R., Curran, T., and McKinnon, P.J. (2007). Loss of suppressor-of-fused function promotes tumorigenesis. Oncogene *26*, 6442–6447.

Legué, E., Gottshall, J.L., Jaumouillé, E., Roselló-Díez, A., Shi, W., Barraza, L.H., Washington, S., Grant, R.L., and Joyner, A.L. (2016). Differential timing of granule cell production during cerebellum development underlies generation of the foliation pattern. Neural Dev. *11*, 17.

Leto, K., Arancillo, M., Becker, E.B., Buffo, A., Chiang, C., Ding, B., Dobyns, W.B., Dusart, I., Haldipur, P., Hatten, M.E., et al. (2016). Consensus Paper: Cerebellar Development. Cerebellum *15*, 789–828.

Lewis, P.M., Gritli-Linde, A., Smeyne, R., Kottmann, A., and McMahon, A.P. (2004). Sonic hedgehog signaling is required for expansion of granule neuron precursors and patterning of the mouse cerebellum. Dev. Biol. *270*, 393–410.

Lin, J.C., Cai, L., and Cepko, C.L. (2001). The external granule layer of the developing chick cerebellum generates granule cells and cells of the isthmus and rostral hindbrain. J. Neurosci. *21*, 159–168.

Machold, R., and Fishell, G. (2005). Math1 is expressed in temporally discrete pools of cerebellar rhombic-lip neural progenitors. Neuron *48*, 17–24.

Mille, F., Tamayo-Orrego, L., Lévesque, M., Remke, M., Korshunov, A., Cardin, J., Bouchard, N., Izzi, L., Kool, M., Northcott, P.A., et al. (2014). The Shh receptor Boc promotes progression of early medulloblastoma to advanced tumors. Dev. Cell *31*, 34–47.

Millonig, J.H., Millen, K.J., and Hatten, M.E. (2000). The mouse Dreher gene Lmx1a controls formation of the roof plate in the vertebrate CNS. Nature *403*, 764–769.

Mukhopadhyay, S., and Rohatgi, R. (2014). G-protein-coupled receptors, Hedgehog signaling and primary cilia. Semin. Cell Dev. Biol. *33*, 63–72.

Mukhopadhyay, S., Wen, X., Ratti, N., Loktev, A., Rangell, L., Scales, S.J., and Jackson, P.K. (2013). The ciliary G-protein-coupled receptor Gpr161 negatively regulates the Sonic hedgehog pathway via cAMP signaling. Cell *152*, 210–223.

Northcott, P.A., Korshunov, A., Witt, H., Hielscher, T., Eberhart, C.G., Mack, S., Bouffet, E., Clifford, S.C., Hawkins, C.E., French, P., et al. (2011). Medulloblastoma comprises four distinct molecular variants. J. Clin. Oncol. *29*, 1408–1414.

Northcott, P.A., Buchhalter, I., Morrissy, A.S., Hovestadt, V., Weischenfeldt, J., Ehrenberger, T., Gröbner, S., Segura-Wang, M., Zichner, T., Rudneva, V.A., et al. (2017). The whole-genome landscape of medulloblastoma subtypes. Nature *547*, 311–317.

Pugh, T.J., Weeraratne, S.D., Archer, T.C., Pomeranz Krummel, D.A., Auclair, D., Bochicchio, J., Carneiro, M.O., Carter, S.L., Cibulskis, K., Erlich, R.L., et al. (2012). Medulloblastoma exome sequencing uncovers subtype-specific somatic mutations. Nature *488*, 106–110.

Robinson, G., Parker, M., Kranenburg, T.A., Lu, C., Chen, X., Ding, L., Phoenix, T.N., Hedlund, E., Wei, L., Zhu, X., et al. (2012). Novel mutations target distinct subgroups of medulloblastoma. Nature *488*, 43–48.

Schüller, U., Heine, V.M., Mao, J., Kho, A.T., Dillon, A.K., Han, Y.G., Huillard, E., Sun, T., Ligon, A.H., Qian, Y., et al. (2008). Acquisition of granule neuron precursor identity is a critical determinant of progenitor cell competence to form Shh-induced medulloblastoma. Cancer Cell *14*, 123–134.

Spassky, N., Han, Y.G., Aguilar, A., Strehl, L., Besse, L., Laclef, C., Ros, M.R., Garcia-Verdugo, J.M., and Alvarez-Buylla, A. (2008). Primary cilia are required for cerebellar development and Shh-dependent expansion of progenitor pool. Dev. Biol. *317*, 246–259.

Taylor, M.D., Liu, L., Raffel, C., Hui, C.C., Mainprize, T.G., Zhang, X., Agatep, R., Chiappa, S., Gao, L., Lowrance, A., et al. (2002). Mutations in SUFU predispose to medulloblastoma. Nat. Genet. *31*, 306–310.

Vanner, R.J., Remke, M., Gallo, M., Selvadurai, H.J., Coutinho, F., Lee, L., Kushida, M., Head, R., Morrissy, S., Zhu, X., et al. (2014). Quiescent sox2(+) cells drive hierarchical growth and relapse in sonic hedgehog subgroup medulloblastoma. Cancer Cell *26*, 33–47.

Wallace, V.A. (1999). Purkinje-cell-derived Sonic hedgehog regulates granule neuron precursor cell proliferation in the developing mouse cerebellum. Curr. Biol. *9*, 445–448.

Wang, V.Y., Rose, M.F., and Zoghbi, H.Y. (2005). Math1 expression redefines the rhombic lip derivatives and reveals novel lineages within the brainstem and cerebellum. Neuron *48*, 31–43.

Wechsler-Reya, R.J., and Scott, M.P. (1999). Control of neuronal precursor proliferation in the cerebellum by Sonic Hedgehog. Neuron *22*, 103–114.

Yang, Z.J., Ellis, T., Markant, S.L., Read, T.A., Kessler, J.D., Bourboulas, M., Schüller, U., Machold, R., Fishell, G., Rowitch, D.H., et al. (2008). Medulloblastoma can be initiated by deletion of Patched in lineage-restricted progenitors or stem cells. Cancer Cell *14*, 135–145.

Zhuo, L., Theis, M., Alvarez-Maya, I., Brenner, M., Willecke, K., and Messing, A. (2001). hGFAP-cre transgenic mice for manipulation of glial and neuronal function in vivo. Genesis *31*, 85–94.

Cell Reports, Volume *22*

Supplemental Information

Basal Suppression of the Sonic Hedgehog Pathway by the G-Protein-Coupled Receptor Gpr161 Restricts Medulloblastoma Pathogenesis

Issei S. Shimada, Sun-Hee Hwang, Bandarigoda N. Somatilaka, Xin Wang, Patryk Skowron, Jiwoong Kim, Min Kim, John M. Shelton, Veena Rajaram, Zhenyu Xuan, Michael D. Taylor, and Saikat Mukhopadhyay

Supplementary Experimental Procedures

Mice genotyping and BrdU incorporation

Mice were housed in standard cages that contained three to five mice per cage, with water and standard diet *ad libitum* and 12 h light/dark cycle. For genotyping of *Gpr161*$^{fl/fl}$ mice, following primers were used to detect wild type band (816bp), flox band (965 bp) and deleted band (340bp); P1 (5' CAA GAT GGA TTC GCA GTA GCT TGG 3'), P2 (5' ATG GGG TAC ACC ATT GGA TAC AGG 3'), and P3 (5' CAA CGG GTT CTT CTG TTA GTC C 3'). For genotyping *Cre*, following primers were used to detect transgene band; Cre-F (5' AAT GCT GTC ACT TGG TCG TGG C 3'), Cre-R (5' GAA AAT GCT TCT GTC CGT TTG C 3'). For genotyping *SmoM2*, following primers were used to detect mutant (450bp) and wild type band (297bp); 23230 (5' CAA CAG CCG CAC TAT CAT CA 3'), oIMR8619 (5' CTC CAG ACT GCC TTG GGA AAA 3'), oIMR9020 (5' AAG GGA GCT GCA GTG GAG TA 3'), oIMR9021 (5' CCG AAA ATC TGT GGG AAG TC 3'). For genotyping *Ift88*, following primers were used to detect mutant (410 bp) and wild type band (365 bp); 16967-F (5'-GAC CAC CTT TTT AGC CTC CTG-3'), 16969-R (5'-AGG GAA GGG ACT TAG GAA TGA-3'). To assess cell proliferation, we administered a pulse of BrdU (B5002; Sigma; 50 mg of BrdU/kg body mass dissolved in PBS) injected intraperitoneally 1 h before the mice were killed for analysis.

Tissue processing, antibodies, immunostaining and microscopy

Mice were perfused with PBS, dissected and bisected down the midline, fixed in 4% parafolmaldehyde overnight at 4°C, and processed for cryosection or paraffin embedding and sectioning. For cryosection, the brains were incubated in 30% sucrose for 1-2 days at 4°C. Brains were mounted with OCT compound, and cut into 15 µm frozen sections. For paraffin section, brains were processed over a 12-hour period using a Thermo-Shandon Hypercenter Automated Tissue Processor (A78400001D; ThermoFisher Scientific) which dehydrated the brains through 6 ethanol concentrations, from 50% ethanol to 100% ethanol, cleared through 3 changes of xylene, and infiltrated with wax through 3 Paraplast Plus paraffin baths (39602004; Leica). Samples were embedded in Paraplast Plus using paraffin-filled stainless steel base molds and a Thermo-Shandon Histocenter 2 Embedding Workstation (6400012D; ThermoFisher Scientific). The brains were then cut in 5 µm thick sections, deparafinned and treated with microwave in Antigen Retrieval citra solution (HK086-9K; BioGenex. Fremont, CA) for 13.30 min. For frozen sections, the sections were incubated in PBS for 15 min to dissolve away the OCT. Sections were then blocked in blocking buffer (3% normal donkey serum [Jackson immunoResearch, West Grove, PA], 0.4% Triton X in PBS) for 1 hour at room temperature. Sections were incubated with primary antibodies against the following antigens; overnight at room temperature: Arl13b (1:2000, N295B/66; NeuroMab Facility), BLBP (1:1000, ABN14; Millipore), BrdU (1:500, ab6326; Abcam), Cyclin D1 (1:500, RB-9041-P0, Neomarkers), Doublecortin (DCX; 1:1000, AB5910; Millipore), γH2AX (1:500, 9718; Cell signaling), Gpr161 (custom made) (Pal et al., 2016), Ki67 (1:500, ab1667; Abcam), NeuN (1:500, MAB377; Millipore), P27^{Kip} (P27, 1:500, 610241; BD Biosciences), Pax6 (1:500, 901301; Biolegend), P-Histone H3 (pH3; 1:500, 9706; Cell Signaling), and Zic2 (1:10,000; gift from Stephen Brown, University of Vermont College of Medicine, Burlington). For BrdU staining, sections were treated with 2 N HCl for 15 min at 37°C and washed before incubating with blocking buffer. After three PBS washes, the sections were incubated in secondary antibodies (Alexa Fluor 488-, 555-, 594-, 647- conjugated secondary antibodies, 1:500; Life Technologies, Carlsbad, CA or Jackson ImmunoResearch) for 1 hour at room temperature. Cell nuclei were stained with DAPI (Sigma). Slides were mounted with Fluoromount-G (0100-01; Southern Biotech) and images were acquired with a Zeiss AxioImager.Z1 microscope and a Zeiss LSM780 confocal microscope. Immunohistochemistry was performed with Dako omnis automatic immunohistochemistry machine with following antigens; beta-catenin (GA70261-2; Dako), Gab1 (sc-133191; Santa Cruz Biotechnology), GFAP (GA524; Dako), synaptophysin (IR660; Dako), and Yap (sc-101199; Santa Cruz Biotechnology). For hematoxylin and eosin staining, paraffin sections were stained by hematoxylin and eosin (Hematoxylin 560; 3801575; Leica and Alcoholic Eosin Y 515; 3801615; Leica) using a Sakura DRS-601 x-y-z robotic-stainer (DRS-601; Sakura-FineTek, Torrance, CA). Slides were dehydrated and mounted with Permount (SP15-100; ThermoFisher Scientific).

Quantitative RT-PCR and immunobloting

RNA samples were derived from the cerebellum and medulloblastoma of C57BL/6 mice, *hGFAP-Cre; Gpr161*$^{fl/f}$, *Nestin-Cre; Gpr161*$^{fl/fl}$ mice and littermate controls. RNA was extracted using the GenElute mammalian total RNA purification kit (RTN350; Sigma). Genomic DNA was eliminated by DNase I (D5307; Sigma). cDNA was synthesized by iScript (1708890; Bio-Rad) or M-MLV Reverse Transcriptase (M1427; Sigma). qRT-PCR was performed with SYBR Green Quantitative RT-qPCR Kit (QR0100; Sigma) or Kicqstart One-Step Probe RT-qPCR ReadyMix (KCQS07; Sigma). Reactions were run in ABI 7500 thermocycler (Applied Biosystems). Primer sequences were: *β-actin*-F 5'- CGT CGA CAA CGG CTC CGG CAT G-3', *β –actin*-R 5'-GGG CCT CGT CAC CCA CAT AGG AG-3', *Atoh1*-F 5'-AGT CAA TGA AGT TGT TTC CC-3', *Atoh1*-R 5'-ACA GAT ACT CTT ATC TGC CC-3', *N-Myc*-F 5'-GGA TGA TCT GCA AGA ACC CAG -3', *N-Myc*-R 5'-GTC ATC TTC GTC CGG GTA GAA-3', *Ki67*-F 5'-CAT TGA CCG CTC CTT TAG GTA TGA AG-3', *Ki67*-R 5'-TTG GTA TCT TGA CCT TCC CCA TCA G-3', *Gli2*-F 5'-AGA CTA TTA CCA CCA GAT GAC-3', *Gli2*-R 5'-TGG ACT AGA GAA TCG TGA TG-3', and *Gli3*-F 5'-AGA CCA TGA TAA GAA CAT CCC-3', *Gli3*-R 5'-ATC TGT TGA TGC ATG TGA AG-3'. Following primers and probes were used with Kicqstart qRT-PCR; Single Tube Taqman Gene Expression Assays for *Gpr161* (MM01291057_M1), *β–actin* (MM00607939) and *Ccnd1* (MM043259) (Applied biosystems). *Ptch1*-F 5'-CAG AGT GAC TAC CTC CAT GAC TGT-3', *Ptch1*-R 5'-GCT GGG TGG ACG TAT GCT-3', FAM-TAMRA labeled *Ptch1* probe 5'-CTC CAC CCA CCA CCT CTG CCT-3', *Gli1*-F 5'-GCA GTG GGT AAC ATG AGT GTC T-3' *Gli1*-R 5'-AGG CAC TAG AGT TGA GGA ATT GT-3', FAM-TAMRA labeled *Gli1* probe 5'-CTC TCC AGG CAG AGA CCC CAG C-3'. Embryos were processed for Gli1/3 immunoblotting as described previously (Wen et al., 2010), using Gli3 (AF3690, R&D, 1:1000), α-tubulin (clone DM1A, T6199, Sigma; 1:5000), and Gli1 (L42B10, Cell Signaling; 1:1000) antibodies.

***In situ* hybridization**

Antisense and sense riboprobes were made using the following templates: *Ptch1, Gli1* (gifts from Andrew McMahon lab and Deanna Grant, Andrew Peterson lab), and *Gpr161* (Mukhopadhyay et al., 2013). Plasmids were linearized and *in vitro* transcription was performed using Maxiscript T7/T3 kit (AM1324M, Life technologies) and ^{35}S-UTP (>1,000 Ci/mmol; NEG039H, PerkinElmer). Radioisotopic *in situ* hybridization was performed as previously described (Shelton et al., 2000). Briefly, 5 μm thick paraffin sections were deparaffinized, permeabilized, and acetylated. The sections were hybridized at 70^{o}C for 14 hours with riboprobes diluted in a mixture (50% formamide, 0.75 M NaCl, 20 mM Tris-HCl, pH 8.0, 5 mM EDTA, pH 8.0, 10 mM $NaPO_4$, pH 8.0, 14% dextran sulfate, 1× Denhardt's, and 0.5 mg/ml tRNA). The sections were rinsed with increasing stringency washes, subjected to RNase A (2μg/ml, 30 min at 37^{o}C) and dehydrated prior to dipping in K.5 nuclear emulsion gel (AGP9281; Ilford, UK). Autoradiographic exposure was performed for 21 to 35 days. Photographic development was done with D-19 Developer Substitute and Kodak Fixer (26920-4; 26942, Ted Pella Inc.). Sections were counterstained with hematoxylin, dehydrated with ethanol, cleared with xylene, and cover slipped with Permount mounting medium (SP15, Fisher Chemical). Pictures were taken by a Leica DM2000 photomicroscope equipped with brightfield, and incident-angle darkfield illumination with an Optronics Microfire digital CCD color camera using PictureFrame 3.0 acquisition software (Optronics, Inc. Goleta, CA, USA). Sense control riboprobes was used to establish the level of background signal. Resulting *in situ* hybridization silver-grain signal was imaged with camera settings to produce near binary intensity and contrast.

Analysis of mouse RNAseq data

Three tumors of *GFAP-Gpr161* mice (3-5 months old), two tumors of *GFAP-SmoM2* mice (less than 1 month old), three P7 cerebellums of C57BL/6 mice and two adult cerebellums (2 months old; C57BL/6 mouse and *Gpr161* mouse) were used. mRNA was extracted using the GenElute mammalian total RNA purification kit (RTN350; Sigma). RNAseq libraries per genotype, each from independent mice, were prepared using the TruSeq® Stranded Total RNA library prep kit (RS-122-2301, Illumina). The libraries were sequenced using an Illumina NextSeq500 sequencer (75bp, single-ended). There were 37±23 million reads per library. The libraries were sequenced using an Illumina NextSeq500 sequencer (75bp, single-ended). There were 37±23 million reads per library. The raw reads were mapped to NCBI mouse reference genome GRCm38, downloaded from UCSC genome browser (http://genome.ucsc.edu). STAR (version 2.4.1c) was used for RNA-seq read mapping with default parameter setting. Across 10 samples, 97±2 percent of the reads can be mapped to the genome, while 81.7±2.3 percent reads are uniquely mappable. RSEM (version 1.2.30) was used to quantify gene expression levels in Transcripts Per Million transcripts (TPM). R (version 3.3.1) was used to perform principle component analysis (PCA), regression analysis with build-in packages. Heatmap with hierarchical clustering was generated for all genes with average expression level higher than 1 TPM and variance of expression more than 2 across all 10 samples using R with gplots package. PCA plot was produced by R package FactoMineR (https://github.com/kassambara/factoextra).

Human samples

De-identified human samples used as routine controls for immunohistochemical identification of medulloblastoma subtype analysis were obtained from the Department of Pathology, Children's Medical Center, Dallas with corresponding hematoxylin and eosin stained histologic sections.

References

Mukhopadhyay, S., Wen, X., Ratti, N., Loktev, A., Rangell, L., Scales, S.J., and Jackson, P.K. (2013). The ciliary G-protein-coupled receptor Gpr161 negatively regulates the Sonic hedgehog pathway via cAMP signaling. Cell *152*, 210-223.

Northcott, P.A., Korshunov, A., Witt, H., Hielscher, T., Eberhart, C.G., Mack, S., Bouffet, E., Clifford, S.C., Hawkins, C.E., French, P.*, et al.* (2011). Medulloblastoma comprises four distinct molecular variants. J Clin Oncol *29*, 1408-1414.

Pal, K., Hwang, S.H., Somatilaka, B., Badgandi, H., Jackson, P.K., DeFea, K., and Mukhopadhyay, S. (2016). Smoothened determines beta-arrestin-mediated removal of the G protein-coupled receptor Gpr161 from the primary cilium. J Cell Biol *212*, 861-875.

Shelton, J.M., Lee, M.H., Richardson, J.A., and Patel, S.B. (2000). Microsomal triglyceride transfer protein expression during mouse development. Journal of lipid research *41*, 532-537.

Wen, X., Lai, C.K., Evangelista, M., Hongo, J.A., de Sauvage, F.J., and Scales, S.J. (2010). Kinetics of hedgehog-dependent full-length Gli3 accumulation in primary cilia and subsequent degradation. Mol Cell Biol *30*, 1910-1922.

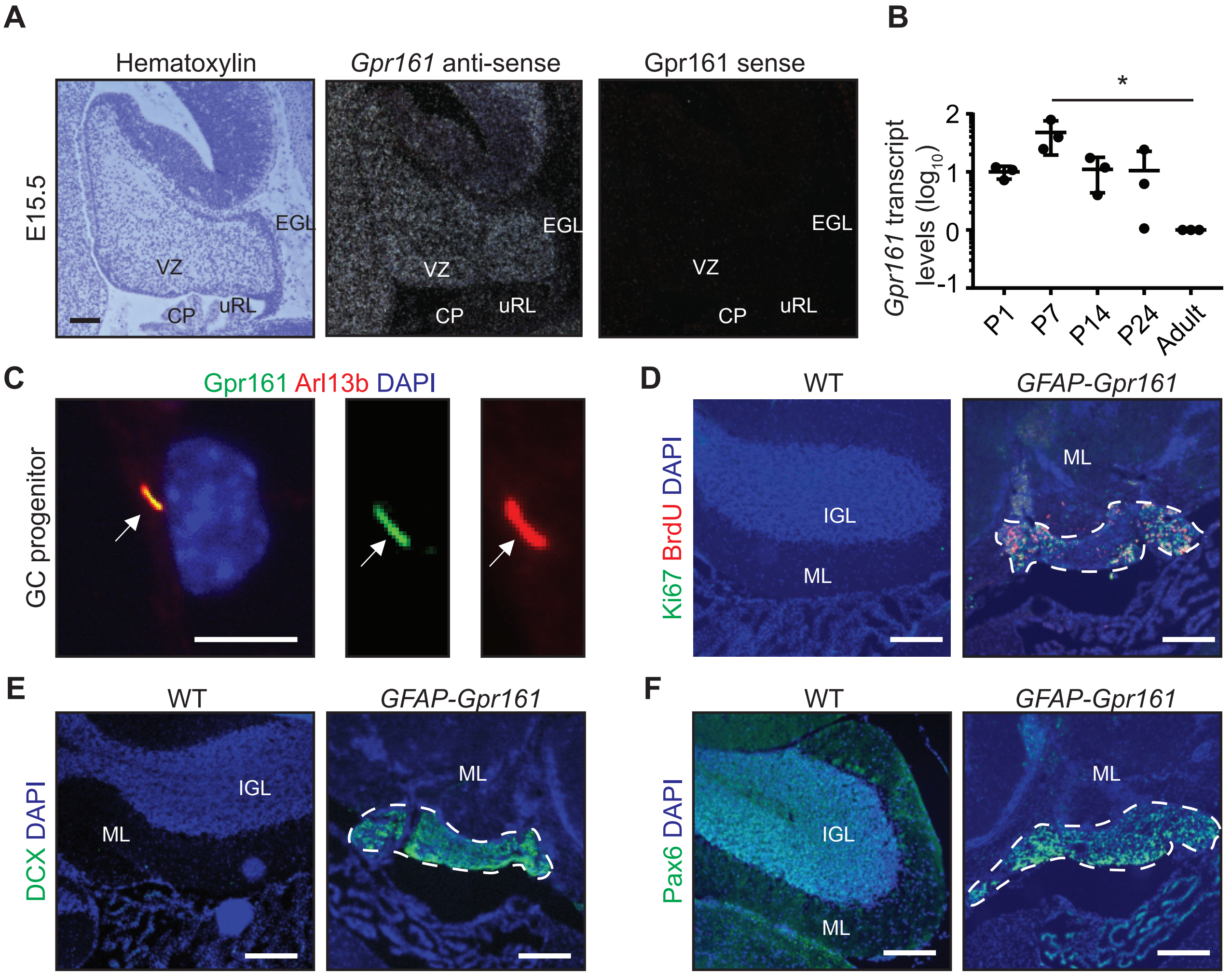

Figure S1. *Gpr161* is expressed in the cerebellum, Related to Figure 1.

(**A**) *In situ* hybridization analysis shows broad expression of *Gpr161* transcripts in the cerebellum at E15.5. Hematoxylin staining shows the morphology of the cerebellum at E15.5.

(**B**) qRT-PCR analysis shows *Gpr161* expression levels during postnatal cerebellum development. Data represents mean ± SD from 3 mice/time point.

(**C**) Co-immunostaining for Gpr161 (green) and Arl13b (red) in primary GC progenitors cultured without Shh pathway activation for 24 h shows Gpr161 localization in primary cilium (marked by Arl13b; white arrow).

(**D**) Representative images of BrdU$^+$ (incorporation after 1 h pulse) and Ki67$^+$ cells in the posterior cerebellum of P50 *GFAP-Gpr161* cko mice shows proliferative region compared to WT without any proliferating cells.

(**E**, **F)** Representative images of DCX$^+$ cells (**E**) and Pax6$^+$ GC progenitors (**F**) in the ventral cerebellum of P50 *GFAP-Gpr161* cko mice and littermate controls.

White dotted line indicates cluster of ectopic cells in the posterior cerebellum.

Abbreviations: ventricular zone (VZ), upper rhombic lip (uRL), external granule layer (EGL), hindbrain choroid plexus (CP). *GFAP-Gpr161* is *hGFAP-Cre; Gpr161*$^{fl/fl}$ and WT represent littermate controls (*Gpr161*$^{fl/fl}$ or *Gpr161*$^{fl/+}$). Scale bars are (**B**) 100 μm (**C**) 10 μm and (**E-F**) 200 μm. Nuclei are stained by DAPI. * $p<0.05$ by Student's *t*-test.

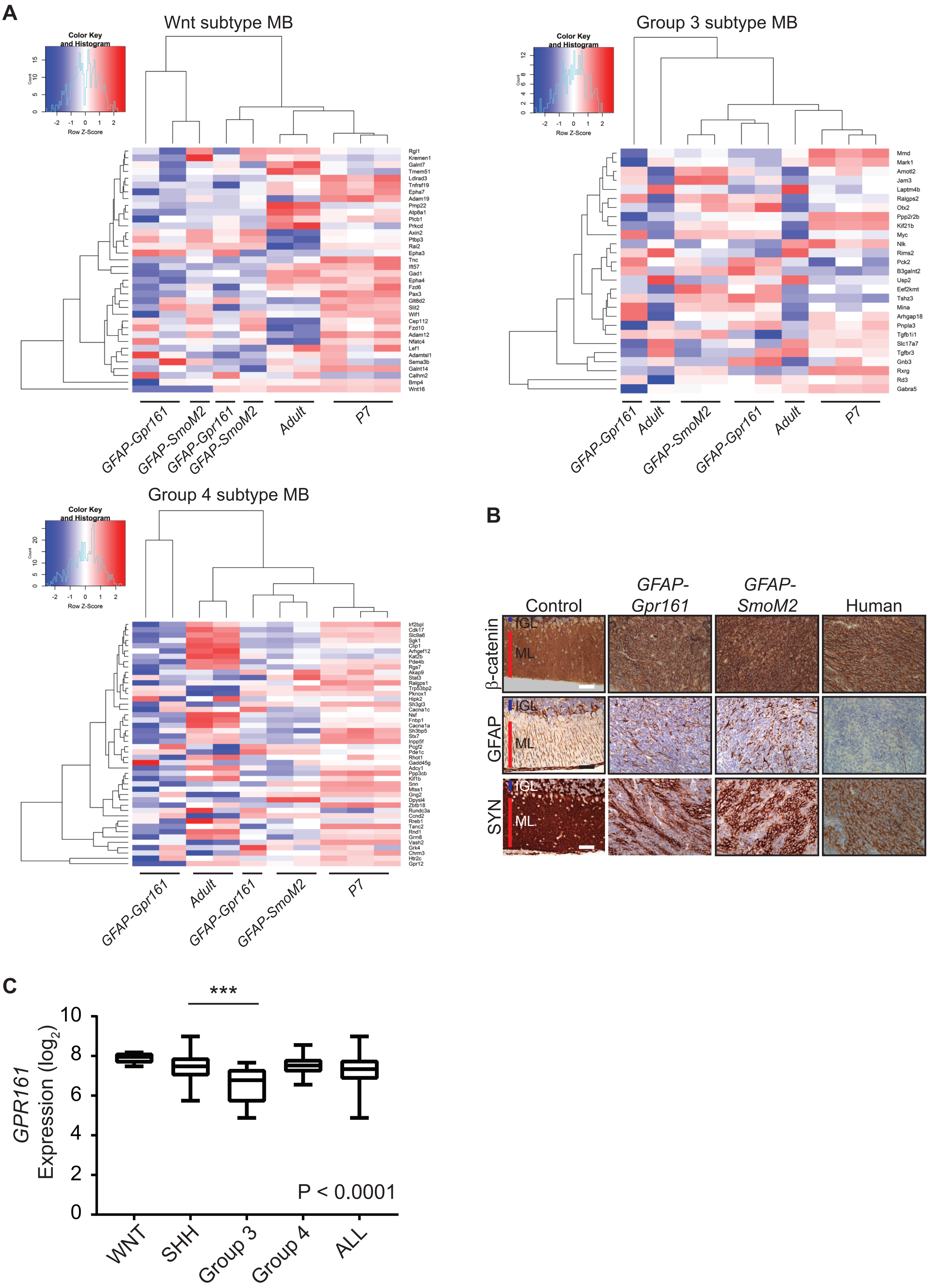
A
Wnt subtype MB
Color Key and Histogram
Count
0
5
10
15
-2
-1
0
1
2
Row Z-Score
Rgl1
Kremen1
Galnt7
Tmem51
Ldlrad3
Tnfrsf19
Epha7
Adam19
Pmp22
Atp8a1
Plcb1
Prkcd
Axin2
Ptbp3
Rai2
Epha3
Tnc
Ift57
Gad1
Epha4
Fzd6
Pax3
Glt8d2
Slit2
Wif1
Cep112
Fzd10
Adam12
Nfatc4
Lef1
Adamtsl1
Sema3b
Galnt14
Calhm2
Bmp4
Wnt16
GFAP-Gpr161
GFAP-SmoM2
GFAP-Gpr161
GFAP-SmoM2
Adult
P7
Group 3 subtype MB
Color Key and Histogram
Count
0
2
4
6
8
12
-2
-1
0
1
2
Row Z-Score
Mmd
Mark1
Amotl2
Jam3
Laptm4b
Ralgps2
Otx2
Ppp2r2b
Kif21b
Myc
Nlk
Rims2
Pck2
B3galnt2
Usp2
Eef2kmt
Tshz3
Mina
Arhgap18
Pnpla3
Tgfb1i1
Slc17a7
Tgfbr3
Gnb3
Rxrg
Rd3
Gabra5
GFAP-Gpr161
Adult
GFAP-SmoM2
GFAP-Gpr161
Adult
P7
Group 4 subtype MB
Color Key and Histogram
Count
0
5
10
20
-2
-1
0
1
2
Row Z-Score
Irf2bpl
Cdk17
Slc9a6
Sgk1
Clip1
Arhgef12
Kat2b
Pde4b
Rgs7
Akap9
Stat3
Ralgps1
Trp53bp2
Pknox1
Hipk2
Sh3gl3
Cacna1c
Nsf
Fnbp1
Cacna1a
Sh3bp5
Stx7
Inpp5f
Pcgf2
Pde1c
Rhot1
Gadd45g
Adcy1
Ppp3cb
Kif1b
Snn
Mtss1
Gng2
Dpysl4
Zbtb18
Rundc3a
Ccnd2
Rreb1
Tanc2
Rnd1
Grm8
Vash2
Grk4
Chrm3
Htr2c
Gpr12
GFAP-Gpr161
Adult
GFAP-Gpr161
GFAP-SmoM2
P7
B
Control
GFAP-Gpr161
GFAP-SmoM2
Human
β-catenin
GFAP
SYN
IGL
ML
IGL
ML
IGL
ML
C
***
10
8
6
4
2
0
GPR161 Expression ($\log_2$)
P < 0.0001
WNT
SHH
Group 3
Group 4
ALL

Figure S2. Gene expression profiles of tumors induced upon *Gpr161* deletion does not resemble other subtypes of medulloblastomas, Related to Figure 2.
(**A**) Heatmap analysis shows that tumors of *GFAP-Gpr161* cko mice do not belong to Wnt-, Group 3-, and Group 4-medulloblastoma subtypes.
(**B**) Immunohistochemical analysis confirms that tumors from *GFAP-Gpr161* cko mice exhibit SHH-subtype-specific staining pattern similar to tumors from *GFAP-SmoM2* mice and human SHH-MB (Human). IGL, Internal granule layer; ML, molecular layer. Note that β-catenin was not localized in the nuclei.
(**C**) Expression levels of *GPR161* separately in WNT-, SHH-, Group 3-, Group 4-subtypes and all subtypes of human medulloblastomas combined (N=8, 33, 27, 36 and 104) (Northcott et al., 2011).
Abbreviations: IGL, Internal granule layer; ML, molecular layer. Significance is calculated by One-way Anova with Sidak's multiple comparisons tests. *** $p < 0.0001$.

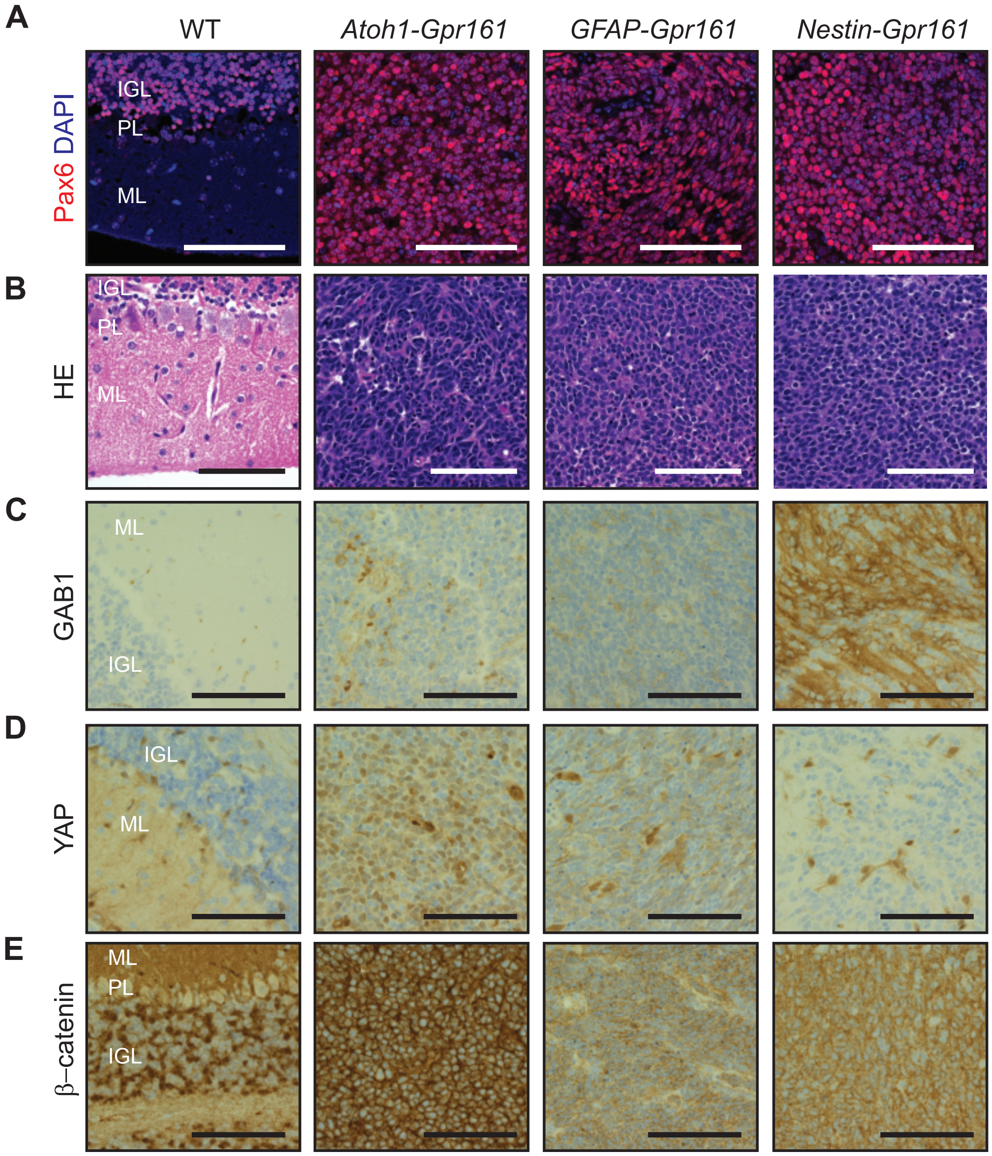

Figure S3. Loss of *Gpr161* in either NSC- or GC- progenitor-specific lineages cause Shh-MB, Related to Figure 3.

(**A**, **C**-**E**) Immunohistochemical analysis shows that tumors of *Atoh1-Gpr161* cko mice *GFAP-Gpr161* cko mice and *Nestin-Gpr161* cko mice exhibit similar staining pattern for (**A**) Pax6, (**C**) YAP, (**D**) β-catenin and (**E**) GAB1.
(**B**) Hematoxylin and eosin stained section of medulloblastomas.
Nuclei are stained by DAPI. Abbreviations: IGL, Internal granule layer; PL, Purkinje Neuron/Bergmann glia layer; ML, molecular layer. *GFAP-Gpr161* is *hGFAP-Cre; Gpr161*$^{fl/fl}$, *Atoh1-Gpr161* is *Atoh1-Cre; Gpr161*$^{fl/fl}$, *Nestin-Gpr161* is *Nestin-Cre; Gpr161*$^{fl/fl}$, and WT is littermate control (*Gpr161*$^{fl/fl}$ or *Gpr161*$^{fl/+}$). Scale bars are (**A**-**E**) 100 um.

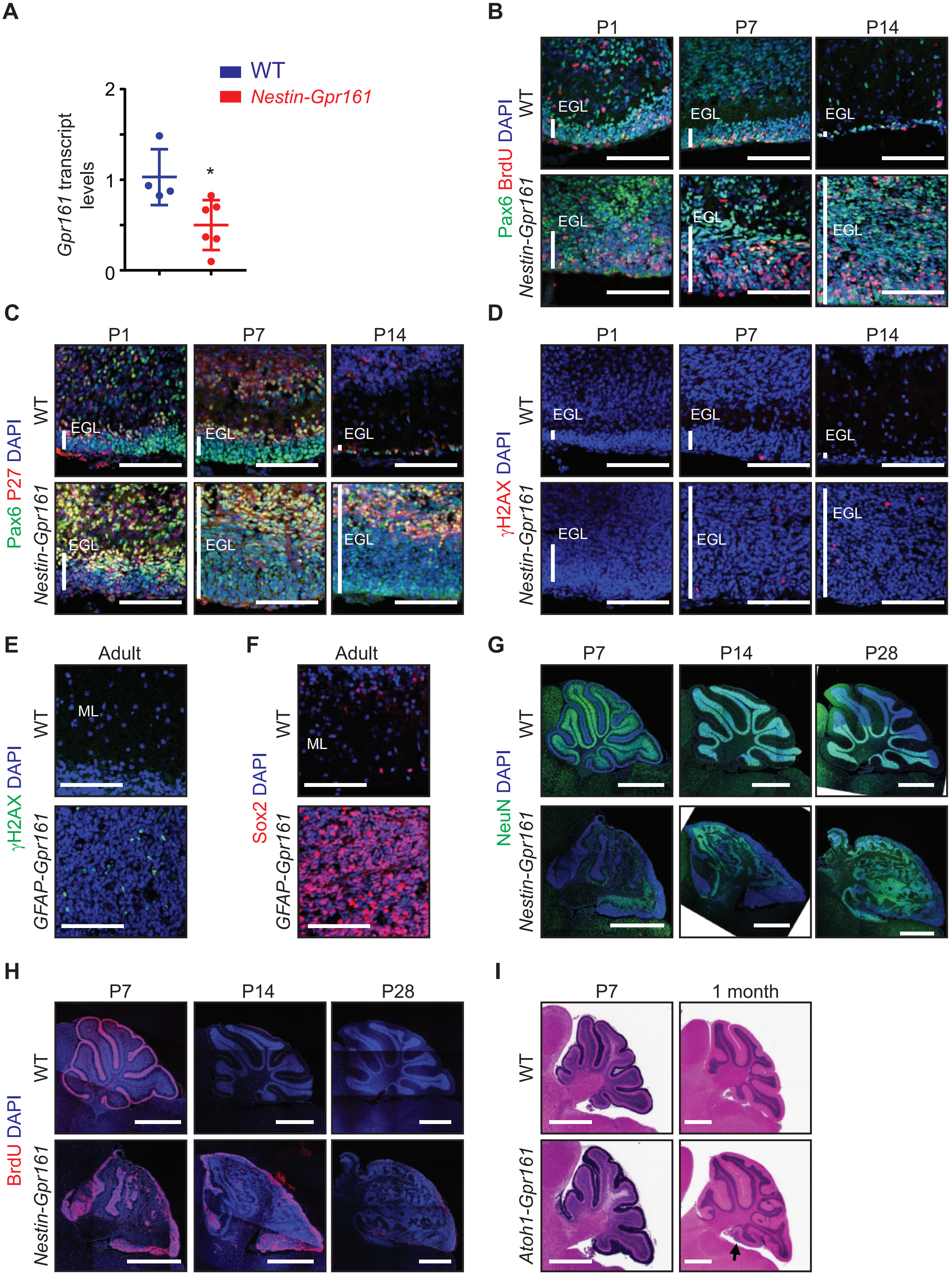
A
WT
Nestin-Gpr161
Gpr161 transcript levels
2
1
0
*
B
P1
P7
P14
Pax6 BrdU DAPI
WT
Nestin-Gpr161
EGL
C
P1
P7
P14
Pax6 P27 DAPI
WT
Nestin-Gpr161
EGL
D
P1
P7
P14
γH2AX DAPI
WT
Nestin-Gpr161
EGL
E
Adult
γH2AX DAPI
WT
GFAP-Gpr161
ML
F
Adult
Sox2 DAPI
WT
GFAP-Gpr161
ML
G
P7
P14
P28
NeuN DAPI
WT
Nestin-Gpr161
H
P7
P14
P28
BrdU DAPI
WT
Nestin-Gpr161
I
P7
1 month
WT
Atoh1-Gpr161

Figure S4. GC progenitor proliferation and dysplasia during postnatal development following *Gpr161* deletion, Related to Figure 4.
(**A**) qRT-PCR analysis shows *Gpr161* transcript levels in the cerebellum of *Nestin-Gpr161* cko mice (N=6) to be significantly decreased compared to that of WT mice (N=4) at P14.
(**B**-**D**) Temporal changes of (**B**) 1 h incorporation of BrdU$^+$ proliferating cells and (**C**) P27$^+$ cells among Pax6$^+$ GC progenitors, and (**D**) γH2AX$^+$ cells in the EGL of *Nestin-Gpr161* cko mice compared to that of WT from P1-P14. Note that the same P14 pictures from Figure 4J, L and M are shown for comparison purpose.
(**E**) γH2AX$^+$ cells in medulloblastoma of *GFAP-Gpr161* cko mouse (6 months old) compared to cerebellum of WT mouse (5 months old) are shown.
(**F**) Sox2$^+$ cells in medulloblastoma of *GFAP-Gpr161* cko mouse (6 months old) compared to cerebellum of WT mouse (5 months old) are shown.
(**G, H**) Gradual changes in proliferation, and accompanying ectopic neurogenesis (dysplasia) in *Nestin-Gpr161* cko mice during postnatal development. Note that unlike WT, *Nestin-Gpr161* cko mice has dysplasia arising from a gradual regression of proliferation into neurogenesis in non-tumor areas, except peripherally and in a few remaining pockets of small proliferative nests.
(**I**) Hematoxylin and eosin staining shows thickened posterior lobe EGL (P7), and ectopic GCs marked by arrow (1 month) in *Atoh1-Gpr161* cko mice.
All data represent mean ± SD. * $p < 0.05$ by Student's *t*-test. Nuclei are stained by DAPI. Abbreviations: *Nestin-Gpr161* is *Nestin-Cre; Gpr161*$^{fl/fl}$, *GFAP-Gpr161* is *hGFAP-Cre; Gpr161*$^{fl/fl}$ and WT represent littermate controls (*Gpr161*$^{fl/fl}$ or *Gpr161*$^{fl/+}$). EGL, external granule layer; ML, molecular layer. Scale bars are (**B**-**F**) 100 um and (**G**, **H, I**) 1 mm. Panels (**G**) and (**H**) are tiled images.

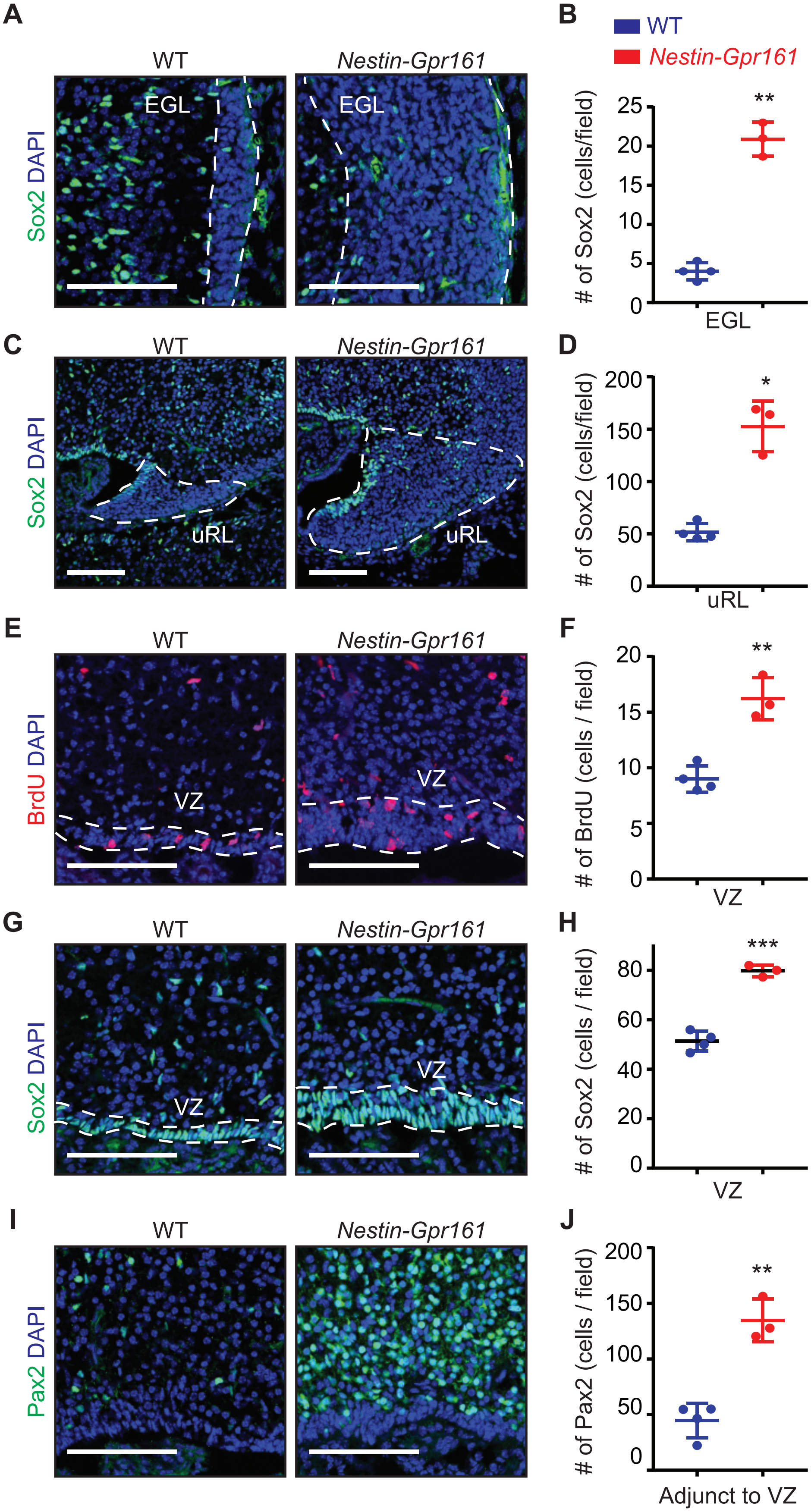
A
WT
Nestin-Gpr161
Sox2 DAPI
EGL
EGL
B
WT
Nestin-Gpr161
# of Sox2 (cells/field)
25
20
15
10
5
0
**
EGL
C
WT
Nestin-Gpr161
Sox2 DAPI
uRL
uRL
D
# of Sox2 (cells/field)
200
150
100
50
0
*
uRL
E
WT
Nestin-Gpr161
BrdU DAPI
VZ
VZ
F
# of BrdU (cells / field)
20
15
10
5
0
**
VZ
G
WT
Nestin-Gpr161
Sox2 DAPI
VZ
VZ
H
# of Sox2 (cells / field)
80
60
40
20
0
***
VZ
I
WT
Nestin-Gpr161
Pax2 DAPI
J
# of Pax2 (cells / field)
200
150
100
50
0
**
Adjunct to VZ

Figure S5. Gpr161 limits NSCs and progenitor cells in the embryonic cerebellum, Related to Figure 5.
(**A**-**D, G,** and **H**) (**A**, **C**, **G**) Representative pictures of Sox2^+ NSCs in the (**A**) EGL, (**C**) uRL (**G**) VZ of *Nestin-Gpr161* cko mice (N=3) and WT mice (N=4) at E16.5. (**B**, **D**, **H**) The number of Sox2^+ NSCs increased in the (**B**) EGL, (**D**) uRL and (**H**) VZ of *Nestin-Gpr161* cko mice compared to that of WT mice.
(**E**, **F**) (**E**) Representative pictures of BrdU$^+$ proliferating cells in the VZ of *Nestin-Gpr161* cko mice (N=3) and WT mice (N=4) at E16.5. (**F**) The number of BrdU$^+$ proliferating cells is increased in the VZ of *Nestin-Gpr161* cko mice compared to that of WT mice.
(**I**, **J**) Representative pictures of Pax2^+ GABAergic neuronal progenitor cells in the area adjacent to VZ of *Nestin-Gpr161* cko mice (N=3) compared to that of WT (N=4) at E16.5. (**J**) The number of Pax2^+ cells is increased in *Nestin-Gpr161* cko mice compared to that of WT mice in this area.
All data represent mean ± SD. Scale bars are (**A**, **C**, **E**, **G**, **I**) 100 µm. Nuclei are stained by DAPI. * $p < 0.05$, ** $p < 0.01$, *** $P<0.001$ by Student's *t*-test. Abbreviations: *Nestin-Gpr161* is *Nestin-Cre; Gpr161*$^{fl/fl}$ and WT is littermate control (*Nestin-Cre; Gpr161*$^{fl/+}$ or *Gpr161*$^{fl/fl}$ or *Gpr161*$^{fl/+}$).

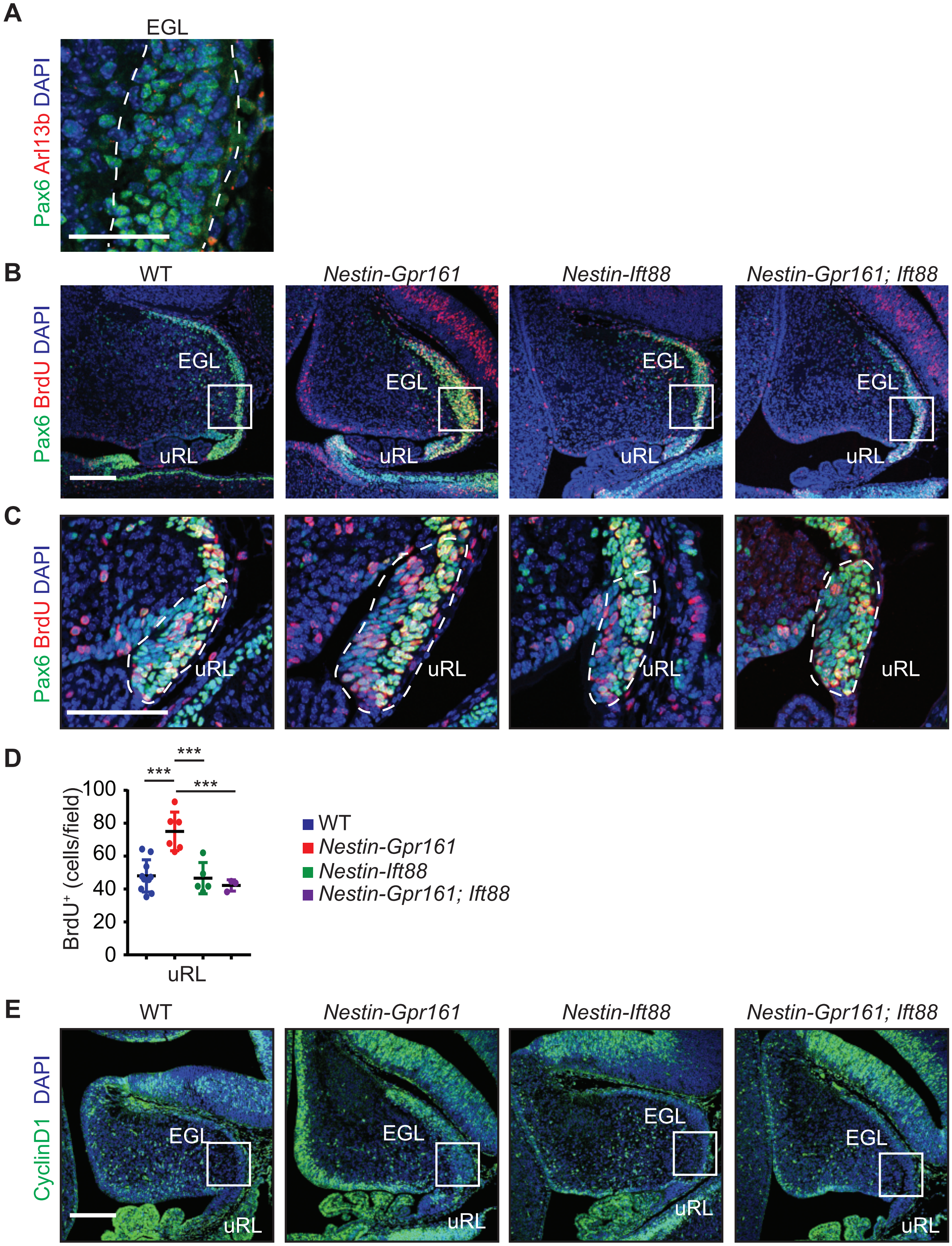
A
EGL
Pax6 Arl13b DAPI
B
WT
Nestin-Gpr161
Nestin-Ift88
Nestin-Gpr161; Ift88
Pax6 BrdU DAPI
EGL
uRL
C
Pax6 BrdU DAPI
uRL
D
BrdU⁺ (cells/field)
100
80
60
40
20
0
***
***
***
uRL
🟦 WT
🟥 Nestin-Gpr161
🟩 Nestin-Ift88
🟪 Nestin-Gpr161; Ift88
E
WT
Nestin-Gpr161
Nestin-Ift88
Nestin-Gpr161; Ift88
CyclinD1 DAPI
EGL
uRL

Figure S6. Gpr161 prevents premature Shh signaling during embryogenesis in a cilia-dependent manner, Related to Figure 7.
(**A**) Pax6^{+} GC progenitors have Arl13b^{+} primary cilia in the EGL of the cerebellum at E15.5.
(**B**-**E**) Representative images of proliferating GC progenitors in the cerebellum (**B**) and uRL (**C**) at E15.5, and the quantification in uRL (**D**). The numbers of mice in (**D**) were WT (N=11), *Nestin-Gpr161* cko mice (N=6), *Nestin-Ift88* cko mice (N=5) and *Nestin-Gpr161;Ift88* dko mice (N=3). (**E**) Representative images of CyclinD1 immunostaining in the cerebellar anlage. Insets shown in (**B**) and (**E**) are shown in high magnification in Figure 7(**C**) and 7(**G**), respectively.
Scale bars are (**A**, **B**, **E**) 200 µm (**C**) 100 µm. Nuclei are stained by DAPI. *** $p < 0.001$ by One-way ANOVA with Sidak multiple comparisons test. Abbreviations: (i) *Nestin-Gpr161* cko is *Nestin-Cre; Gpr161*$^{fl/fl}$*; Ift88*$^{fl/+}$. (ii) *Nestin-Ift88* cko is *Nestin-Cre; Ift88*$^{fl/fl}$*; Gpr161*$^{fl/+}$. (iii) *Nestin-Gpr161; Ift88* dko is *Nestin-Cre; Gpr161*$^{fl/fl;}$ *Ift88*$^{fl/fl}$. WT is littermate control (*Nestin-Cre; Gpr161*$^{fl/+}$*; Ift88*$^{fl/+}$ or *Gpr161*$^{fl/fl}$*; Ift88*$^{fl/fl}$, or *Gpr161*$^{fl/+}$*; Ift88*$^{fl/fl}$, or *Gpr161*$^{fl/fl}$*; Ift88*$^{fl/+}$). EGL, external granule layer; uRL, upper rhombic lip; VZ, ventricular zone.